

A 1200- μm MAMBO survey of the GOODS-N field: a significant population of submillimetre drop-out galaxies

Thomas R. Greve,^{1,2} Alexandra Pope,^{3,4} Douglas Scott,³ Rob. J. Ivison,^{5,6} Colin Borys,² Christopher J. Conselice⁷ and Frank Bertoldi⁸

¹Max-Planck Institute für Astronomie, Königstuhl 17, Heidelberg 69117, Germany

²California Institute of Technology, Pasadena, CA 91125, USA

³Department of Physics & Astronomy, University of British Columbia, Vancouver, BC V6T1Z1, Canada

⁴Spitzer Fellow; National Optical Astronomy Observatory, 950 North Cherry Avenue, Tucson, AZ 85719, USA

⁵UK Astronomy Technology Centre, Royal Observatory, Blackford Hill, Edinburgh EH9 3HJ

⁶Institute for Astronomy, University of Edinburgh, Blackford Hill, Edinburgh EH9 3HJ

⁷University of Nottingham, School of Physics & Astronomy, Nottingham NG7 2RD

⁸Argelander Institute for Astronomy, University of Bonn, Auf dem Hügel 71, 53121 Bonn, Germany

Accepted ... ; Received ... ; in original form ...

ABSTRACT

We present a 1200- μm image of the Great Observatories Origin Deep Survey North (GOODS-N) field, obtained with the Max Planck Millimeter Bolometer array (MAMBO) on the IRAM 30-m telescope. The survey covers a contiguous area of 287 arcmin² to a near-uniform noise level of ~ 0.7 mJy beam⁻¹. After Bayesian flux deboosting, a total of 30 sources are recovered ($\geq 3.5\sigma$). An optimal combination of our 1200- μm data and an existing 850- μm image from the Submillimetre Common-User Bolometer Array (SCUBA) yielded 33 sources ($\geq 4\sigma$). We combine our GOODS-N sample with those obtained in the Lockman Hole and ELAIS N2 fields (Scott et al. 2002; Greve et al. 2004) in order to explore the degree of overlap between 1200- μm - and 850- μm -selected galaxies (hereafter SMGs), finding no significant difference between their $S_{850\mu\text{m}}/S_{1200\mu\text{m}}$ distributions. However, a noise-weighted stacking analysis yields a significant detection of the 1200- μm -blank SCUBA sources, $S_{850\mu\text{m}}/S_{1200\mu\text{m}} = 3.8 \pm 0.4$, whereas no significant 850- μm signal is found for the 850- μm -blank MAMBO sources ($S_{850\mu\text{m}}/S_{1200\mu\text{m}} = 0.7 \pm 0.3$). The hypothesis that the $S_{850\mu\text{m}}/S_{1200\mu\text{m}}$ distribution of SCUBA sources is also representative of the MAMBO population is rejected at the $\sim 4\sigma$ level, via Monte Carlo simulations. Therefore, although the populations overlap, galaxies selected at 850 and 1200 μm are different, and there is compelling evidence for a significant 1200- μm -detected population which is not recovered at 850 μm . These are submm drop-outs (SDOs), with $S_{850\mu\text{m}}/S_{1200\mu\text{m}} = 0.7 - 1.7$, requiring very cold dust or unusual spectral energy distributions ($T_d \simeq 10$ K; $\beta \simeq 1$), unless SDOs reside beyond the redshift range observed for radio-identified SMGs, i.e. at $z > 4$.

Key words: surveys: galaxies – galaxies: starburst – galaxies: formation – galaxies: evolution – cosmology: observations – cosmology: submillimetre

1 INTRODUCTION

A decade ago, surveys undertaken at submillimetre (submm; 850- μm) wavelengths with SCUBA (Holland et al. 1999) transformed the accepted understanding of galaxy formation and evolution by revealing an unexpected yet significant population of dusty, far-infrared-luminous starburst galaxies (Smail, Ivison & Blain 1997; Hughes et al. 1998; Barger et al. 1998). Since then, great strides have been made in understanding the nature of submm-selected galaxies – see Blain et al. 2002 for a review – largely facilitated by accurately pinpointing SMGs in deep, high-resolution radio maps (e.g. Ivison et al. 1998a, 2000, 2002; Smail et al. 2000) which helps overcome the coarse resolution of SCUBA (FWHM $\simeq 15$ arcsec). The majority (60–80 per cent) of bright ($S_{850\mu\text{m}} \gtrsim 5$ mJy) SMGs have been identified in this way and one of the most important

steps forward was the acquisition of about 100 optical/near-infrared spectra of such radio-identified SMGs. This placed them typically in the redshift range $z \simeq 1-3$, with a median of 2.3 (Chapman et al. 2003, 2005). However, while submm surveys are equally sensitive to sources of a fixed luminosity in the redshift range $z \simeq 1-8$, due to the negative k -correction offsetting the cosmic dimming (Blain & Longair 1993), the detection rate of SMGs in even the deepest radio surveys drops off rapidly beyond $z \simeq 3.5$. Thus, the spectroscopic requirement for a robust radio detection biases the known population to $z \lesssim 3.5$. This led to the suggestion that the 20–40 per cent of the bright, radio-blank SMGs (1.4 GHz flux density, $S_{1.4\text{GHz}} \lesssim 20$ μJy) could be the high-redshift tail of the population ($z > 4$ – see Carilli & Yun 1999; Ivison et al. 2002; Eales et al. 2003; Aretxaga et al. 2003, 2007), although using photometric

redshifts Pope et al. (2006) argued that <14 per cent of the bright SMG population is at $z > 4$.

Perhaps the strongest candidates for $z > 4$ SMGs have come from submm/mm interferometry, with the IRAM Plateau de Bure Interferometer (PdBI) and the Submillimeter Array (SMA), of a few very bright SMGs which – by virtue of their radio, submm/mm and near-infrared properties – were deemed to reside at very high redshift (Dannerbauer et al. 2002; Wang et al. 2007; Younger et al. 2007).

Soon after the first observations with SCUBA, surveys were being conducted at 1200 μm with MAMBO (Bertoldi et al. 2000) resulting in samples of sources that were thought to be identical to SMGs, except selected at mm wavelengths. Compared to submm surveys, however, observations at mm wavelengths should be sensitive to far-IR-luminous galaxies out to higher redshifts, due to the k -correction, as well as to systems with cooler dust temperatures. As a result, at $z \gtrsim 3$ the 850-/1200- μm flux ratio becomes a relatively strong function of redshift for a typical starburst far-infrared/mm spectral energy distribution (SED), and may therefore (if the SED is known) be used as a crude redshift estimator or – if the redshift is known – as an indicator of the shape (i.e. temperature and spectral index) of the far-infrared/mm SED.

This fact was exploited by Eales et al. (2003; hereafter E03), who obtained 850- μm photometric measurements of a sample of 1200- μm -selected sources and found a significant fraction to have very low 850/1200- μm flux ratios ($S_{850\mu\text{m}}/S_{1200\mu\text{m}} \lesssim 2$). They argued that this was either indicative of SMGs at $z \gg 3$ or – since a large fraction of their sample was radio-identified with radio-to-submm flux ratios consistent with $z \leq 3$ – SMGs having fundamentally different dust emission properties than local galaxies. The existence of a significant number of these SDOs, which we define here as sources with $S_{850\mu\text{m}}/S_{1200\mu\text{m}} \lesssim 2$, was questioned (albeit not ruled out) by Greve et al. (2004; hereafter G04), who performed the first unbiased comparison of 850- and 1200- μm -selected sources, using catalogues extracted from SCUBA and MAMBO maps. The degree of overlap between source populations extracted from submm and mm surveys (and in particular the idea that mm observations are tracing a significant sub-population of more distant and/or cooler sources) remains controversial, therefore, and is further complicated by the difficulty of comparing (sub)mm surveys with different depths and noise properties. Nonetheless, settling this issue is important; regardless of the outcome, it tells us about the population of dusty galaxies at the highest redshifts, with significant implications for our understanding of galaxy formation and evolution.

In this paper we present an unbiased 1200- μm MAMBO survey of the northern field of the Great Observatories Origins Deep Survey (GOODS-N – Giavalisco et al. 2004). As well as presenting the 1200- μm map and source catalogue, we also perform a rigorous comparison between our data and the existing 850- μm SCUBA map of this region (Borys et al. 2003; Pope et al. 2005), in order to address the issues outlined above. In a follow-up paper, we shall exploit other high-quality data in the GOODS-N field to explore the multi-wavelength properties of 1200- μm selected sources.

Throughout this paper we have adopted a flat cosmology with $\Omega_M = 0.27$, $\Omega_\Lambda = 0.73$, and $H_0 = 71 \text{ km s}^{-1} \text{ Mpc}^{-1}$ (Spergel et al. 2003).

2 OBSERVATIONS AND DATA REDUCTION

A 1200- μm (250-GHz) map covering the entire GOODS-N region was obtained using the 117-channel bolometer array, MAMBO (Kreysa et al. 1998), on the IRAM 30-m telescope on Pico Veleta in Spain. The data were obtained during the winter semester 2005-06 in good weather conditions, meaning 250-GHz opacities of $\lesssim 0.3$ and stable atmospheric conditions (low sky-noise).

In order to map the entire field as uniformly as possible, a number of regular grid positions (2 arcmin apart) were observed. Specifically, each such grid position was observed twice, using a standard on-the-fly 300 arcsec \times 320 arcsec Az–Alt scan-map. With a scanning speed of 5 arcsec s^{-1} in Az and an elevation spacing between each sub-scan of 8 arcsec, a scan-map takes ~ 43 min to complete, allowing for a 3-s turnaround after each sub-scan. To avoid any systematics and to minimise the effects of sky rotation, we tried to observe each grid position once when the field was rising and once when it was setting. Different wobbler throws (36–45 arcsec) and scan directions (increasing or decreasing elevation) were also employed for different scan-maps. In total, 53 scan-maps were obtained.

After each scan-map, a pointing observation on a nearby, bright point source was carried out and, in order to be extra cautious, a focus correction was usually applied after each scan (sometimes after two scans if the focus appeared stable). Since the weather conditions were generally stable, it was sufficient to perform a skydip every 2 hr in order to monitor the 250-GHz atmospheric opacity. Skydips were carried out at the same azimuth as the preceding grid-point observation, ensuring that the opacity was measured for the same part of the sky as the science observations.

The data were reduced with the MOPSIC software – an improved version of the original MOPSI package (Zylka 1998) – using standard pipeline scripts designed to deal with MAMBO data. This involved many of the standard steps in reducing bolometer data, i.e. de-spiking, flat-fielding, removal of correlated noise across the array (see G04 for details), and correction for atmospheric opacity by interpolating between the skydip measurements. The timestream data were rebinned onto a 1 arcsec \times 1 arcsec grid using a shift-and-add technique, which results in each positive source being bracketed by two negative counter-images, each with half of the peak positive intensity, located one wobbler throw away, i.e. the standard ‘double-difference’ or ‘triple-beam’ pattern. However, the different wobbler throws and scanning directions employed for different scans ensure that the negative images are averaged out, resulting in a very clean image (although with some residual effects, discussed in § 3.1).

The final 1200- μm signal-to-noise (hereafter S/N) map and corresponding noise map are shown in Fig. 1. The area covered is 287 arcmin². The map exhibits a fairly uniform r.m.s. noise of $\sim 0.7 \text{ mJy beam}^{-1}$ over most of its area (apart from at the edges where the noise is larger, $\gtrsim 0.8 \text{ mJy beam}^{-1}$).

3 THE GOODS-N 1200-MICRON SOURCE CATALOGUE

3.1 Source extraction

In order to extract sources, a point spread function (PSF) was fitted to each pixel in the map and a S/N ratio was ascribed, based on the local noise. This is similar to the noise-weighted convolution technique applied to MAMBO maps by G04 and to SCUBA maps by Borys et al. (2003) and Coppin et al. (2006). Unlike SCUBA, where one can configure the nod/chop such that it remains constant

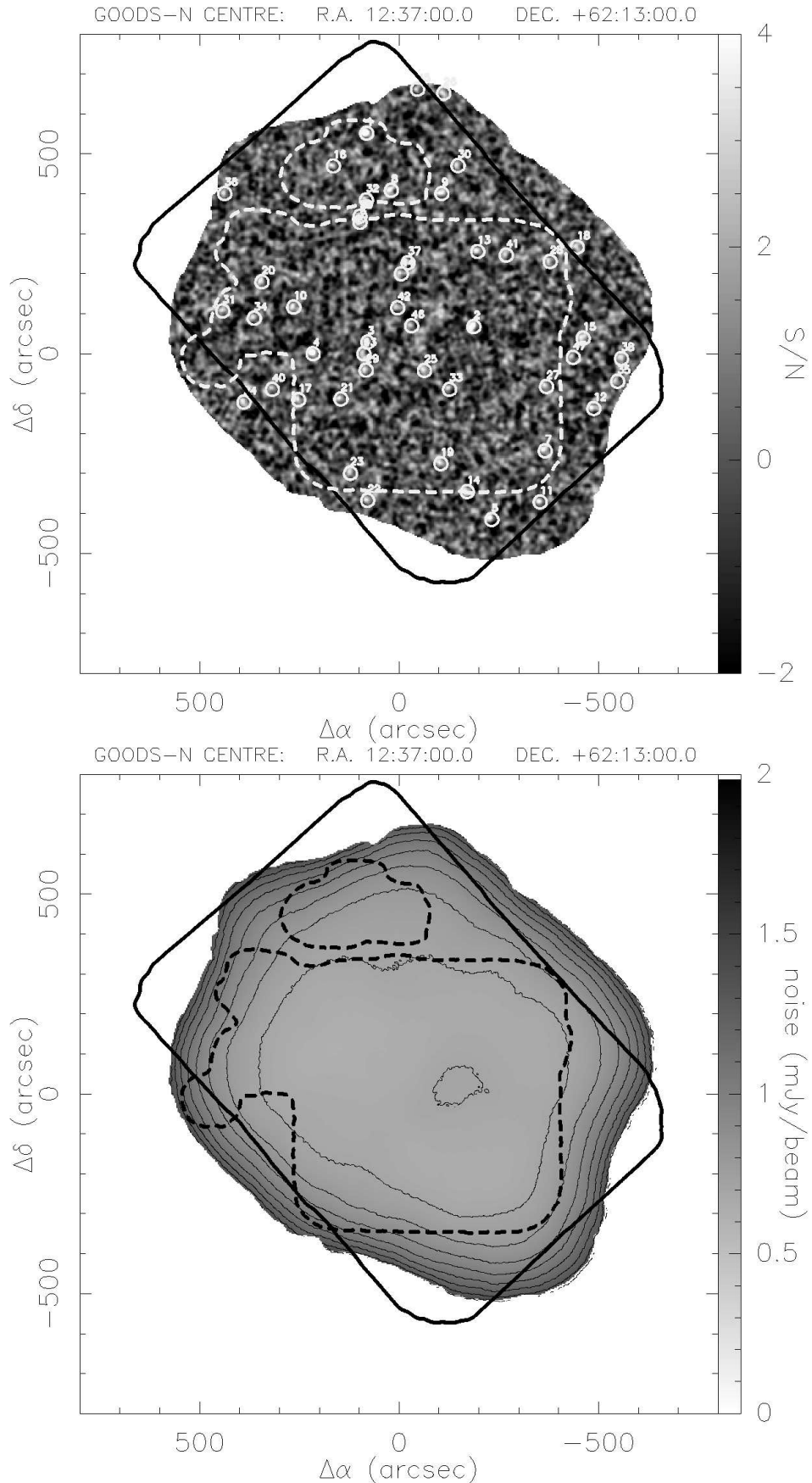


Figure 1. Top: The 1200- μm MAMBO S/N map of the GOODS-N region. Sources extracted at $\geq 3.5\sigma$ (prior to deboosting, see §3.2.3) are indicated as white circles. **Bottom:** The corresponding r.m.s. noise map. The thin black contours correspond to $\sigma = 0.7, \dots, 1.2 \text{ mJy beam}^{-1}$. The thick black outline shows the full extent of the GOODS-N field as observed with *Spitzer*/IRAC and the thick dashed line shows the extent of the SCUBA map (Borys et al. 2003; Pope et al. 2005).

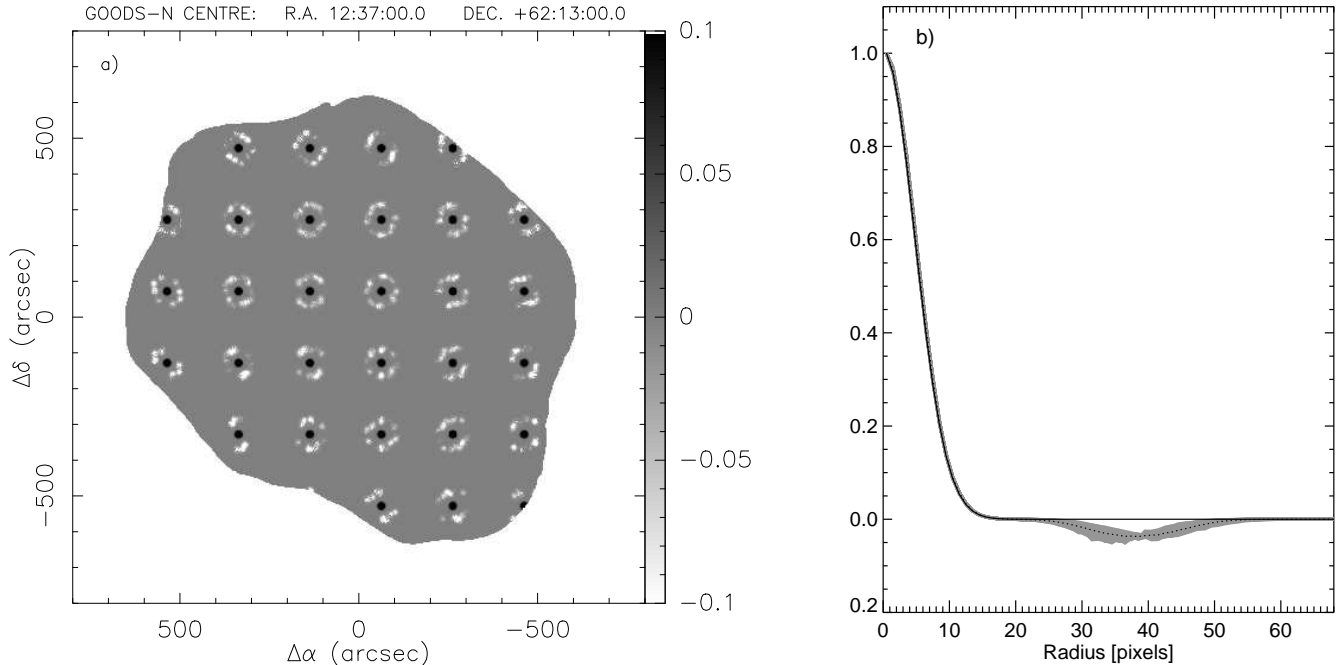


Figure 2. **a)** Variations in the PSF at a collection of grid points across the map. The negative parts of the PSF (shown in white) are caused by the wobbler throw used in the on-the-fly mapping mode on the IRAM 30-m telescope. Due to sky rotation and variations in the chop throw (between 36 and 45 arcsec) the negative residuals are smeared out in a ring around the main beam. **b)** Azimuthally averaged PSF profiles. The gray-shaded region shows the radially averaged profiles of all the PSFs plotted on the left, and the dotted line is the average of those profiles. The solid line is a best-fit Gaussian with a fixed FWHM of 11.1 arcsec.

on the sky, MAMBO experiences sky rotation; as a result, the PSF varies across the map.

We have gone to great lengths to average out the negative chop patterns (see § 2), but we still expect to see some effects of the chop throw in the map. To quantify this, we created fake, noiseless time streams of data, containing a number of point sources at certain positions in the map, and then subjected these data to exactly the same data-reduction pipeline as the real data, using the astrometrical information (coordinates, chop throws etc.) of the real data to create a map which shows how the PSF varies across the map (Fig. 2a).

Ideally, one would want to use the PSF (including its negative parts) as the filtering kernel in the source-extraction procedure, as has been done with SCUBA maps (e.g. Scott et al. 2002, hereafter S02; Borys et al. 2003; Coppin et al. 2006). In our case, that would entail computing a separate PSF for every pixel in the map, or at least some sub-region of the map where the PSF is approximately constant. However, as seen in Fig. 2a, the negative features of the net PSF are fairly low contrast, spread out over a large area, making it difficult (and also largely unnecessary) to use them explicitly in the source-extraction procedure.

This also suggests that the optimal method of combining the data, using an explicit PSF for each individual time sample (see Borys et al. 2003), would produce only marginally better results, at the expense of enormously increased complexity. Indeed, we used a few sources to show that the improvement was modest. We therefore decided to use a simple Gaussian (FWHM, 11.1 arcsec) as an approximation to the PSF. Although the 30-m telescope’s beam is formally 10.7 arcsec FWHM at $1200\ \mu\text{m}$, we have adopted a slighter broader PSF in order to account for the typical pointing error (~ 3 arcsec r.m.s.). That this is, in fact, a good approximation is demonstrated in Fig. 2b where we have plotted the mean

azimuthally averaged PSF profiles, along with a Gaussian profile with FWHM = 11.1 arcsec. While half of the signal is contained in the negative residuals, it is seen that the depth of the negative holes reach only about 5 per cent of the primary PSF height. This procedure yielded 20 sources with $S/N \geq 4$ and a further 27 sources with $3.5 \leq S/N < 4$ (see Table 1).

3.2 Monte Carlo simulations

3.2.1 Spurious sources

In order to assess the degree to which the extracted source catalogue is contaminated by spurious noise peaks, we randomised the bolometer positions on the array in order to create a scrambled map with no sources, with noise properties similar to that of the real map. In total, 500 such scrambled maps were produced, each processed by the data-reduction pipeline in exactly the same way as the real data. Fig. 3 shows the average number of spurious detections in the scrambled maps, when subjected to our source-extraction technique. The simulations suggest that for $\geq 4\text{-}\sigma$ sources extracted from the $287\ \text{arcmin}^2$ surveyed, less than two are expected to be spurious, while we can expect about seven spurious sources in the $3.5\text{-}\sigma$ catalogue. This is in agreement with similar simulations by G04. Fig. 3 also shows how the expected number of spurious sources is larger than for purely uniform Gaussian noise, confirming that it is important to carry out the simulations with realistic noise.

A further check on the source robustness can be made by extracting sources from an inverted map, in other words, carrying out the same extraction procedure for *negative* sources, which of course can only be real when created by freak alignments of sources and chop throws. In total, we find 33 sources above $3.5\ \sigma$ in the inverted

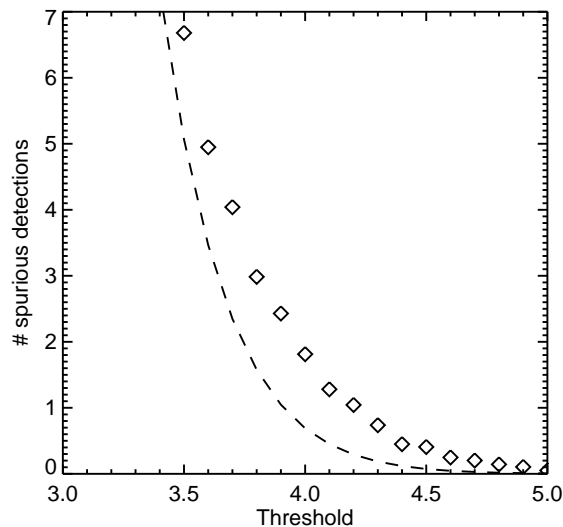


Figure 3. Diamonds show the average number of (positive) spurious detections as a function of S/N ratio, based on simulated maps with realistic noise properties. The dashed line shows the expected number of spurious sources, assuming purely Gaussian noise and a Gaussian beam with a FWHM of 11.1 arcsec.

map. All but six are associated with the negative beams of bright positive sources, consistent with expectations.

3.2.2 Completeness and positional offsets

Catalogue completeness varies as a function of the source flux, becoming smaller at lower flux values. In addition, random noise fluctuations result in the extracted positions being offset from the true source positions; again, the effect becomes increasingly severe at lower fluxes. The effect of the noise on the completeness of the survey and on the positional offsets was assessed using Monte Carlo simulations. Artificial sources with fluxes in the range 1–12 mJy (in steps of 0.25 mJy) were added to the science map, one at a time, at random positions, and subsequently extracted using exactly the same technique used in § 3.1. This procedure was repeated 50 times for every flux bin, each time at a random position in the map. Each injected source was a scaled version of the local PSF and as a result the shape and depth of the negative lobes around the sources was a function of the map position. We also excluded artificial sources which were within half a beam width of any real source, hence this definition of completeness is intended only to assess the effects of noise, without including the effects of confusion (Blain, Ivison & Smail 1998).

The resulting completeness curve and positional offsets are shown in Fig. 4. The simulations suggest that the survey is close to complete down to a flux density of about 3 mJy, and drops precipitously below 2.5 mJy. The lower panel of Fig. 4 shows that the positions of sources with flux densities larger than 2.5 mJy are determined to within 3 arcsec. Of course, in addition to the positional offsets shown in Fig. 4, the data will contain offsets due to pointing errors. The completeness fractions and positional offsets we obtain here are very similar to those found by G04.

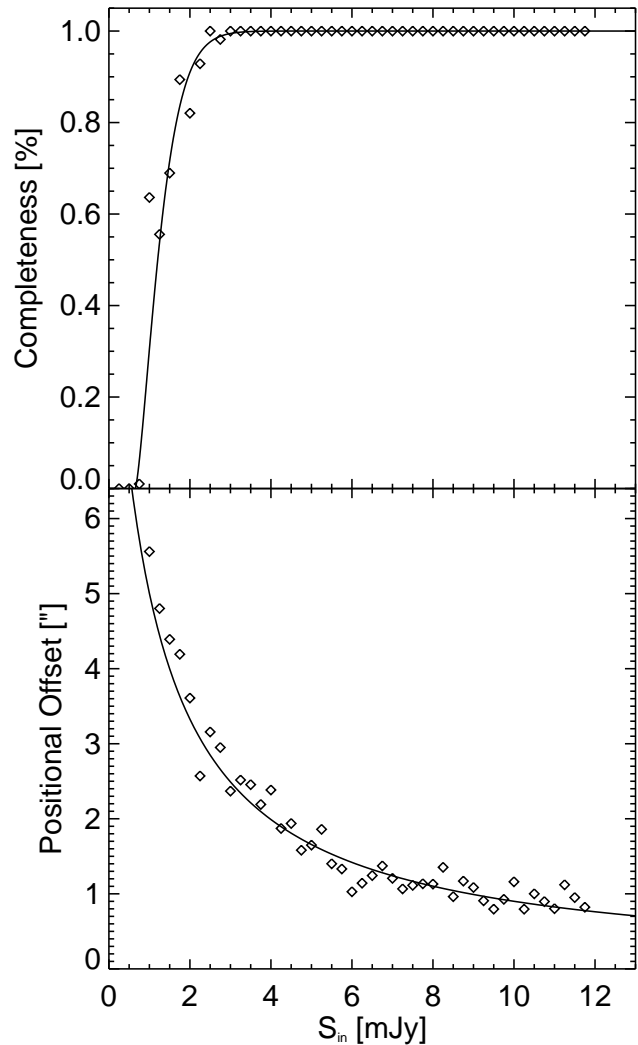


Figure 4. Top: The completeness function of our survey, derived as the percentage of input sources which are recovered by the source extraction as a function of the source flux density (but not including the effects of confusion). The solid curve represents a fit to the phenomenological expression: $f(S_{\text{in}}) = 1 - \exp(A(S_{\text{in}} - B)^C)$. **Bottom:** The positional offsets between the actual positions of the input sources and their extracted position. A fit to the function $f(S_{\text{in}}) = 1 + A \exp(B S_{\text{in}}^C)$ is shown by the solid curve.

3.2.3 Flux deboosting

For any flux-limited survey in the low-S/N regime (as is the case for all submm/mm surveys undertaken to date), we must worry about the superposition of sources with positive noise peaks in the map: ‘flux boosting’ (S02). This effect is particularly significant in the submm/mm waveband where the source number counts have a steep negative slope, so that the noise excursions above a threshold do not balance excursions below the threshold.

We chose to follow the Bayesian flux deboosting approach developed by Coppin et al. (2005) to deal with SCUBA data. The philosophy of this method is to assume *a priori* knowledge of the pixel brightness distribution, $N(S_p)$, in the *noiseless* map. If the noise in the map is Gaussian, the probability of measuring a flux density $S_m \pm \sigma_m$ at some pixel in the map when its true flux is S_p , is

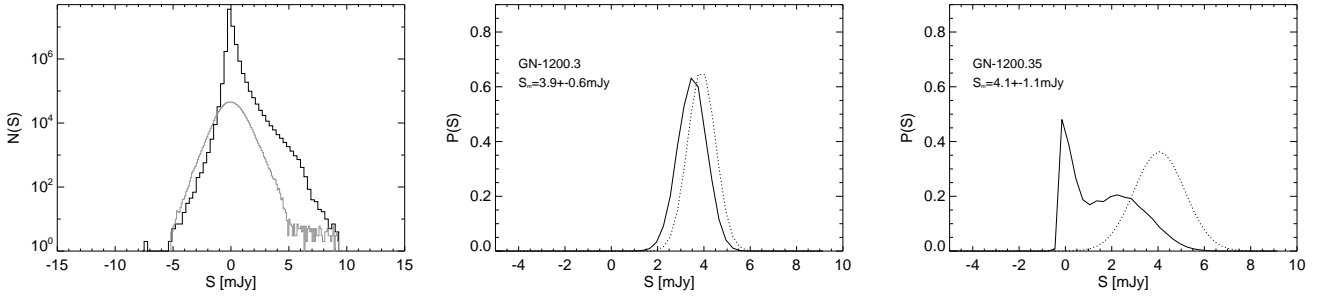


Figure 5. **Left:** The prior flux density probability distribution, $N(S_p)$, of 1,000 simulated maps. Whilst strongly peaked around zero, the distribution is skewed towards positive fluxes due to the presence of sources in the maps. The flux density distribution of the real map is shown in grey. **Middle:** Observed flux density probability distribution (dotted curve) assuming Gaussian errors, $P_M(S_p)$, and the posterior flux density probability distribution (dark solid curve), $P(S_p)$, for the source MM J123711+621328 (GN 1200.3), which is well detected. **Right:** An example of a source, MM J123541+621150 (GN 1200.35), which is less well detected. In this case the posterior flux density distribution peaks at zero and the posterior probability for having zero flux density is larger than 5 per cent. Hence this source does not meet our detection criterion, after deboosting.

$$P_M(S_p) \propto \exp\left(-\frac{(S_m - S_p)^2}{2\sigma_m^2}\right). \quad (1)$$

We can then use Bayes' theorem to derive the probability that the true flux of the pixel is S_p :

$$P(S_p) = \frac{N(S_p)P_M(S_p)}{P(M)}, \quad (2)$$

where $P(M)$ is simply the normalisation constant. The *a priori* flux density distribution, $N(S_p)$, was generated by making noiseless maps onto which sources selected from a model of the number counts were randomly distributed, and then sampled with the adopted chop pattern. In our case, the chop pattern varies across the map so the overall $N(S_p)$ distribution was derived from noiseless maps created with exactly the same scanning strategy as the real map. For the number counts, we adopted a Schechter function of the form $dN/dS \propto (S/S_0)^{-\alpha} \exp(-S/S_0)$, where $S_0 = 4$ mJy and $\alpha = 2.3$; this provides a good fit to the 1200- μ m number counts by G04. The $N(S_p)$ distribution derived from 1,000 such maps is shown in the left panel of Fig. 5. We checked that the use of moderately different number count models has little effect on our results; one has to considerably alter the faint-end slope in order to make significant changes. Examples of deboosting are given in Fig. 5, which shows the probability distribution of the measured flux $P_M(S_p)$ (assuming it is Gaussian) and the corresponding deboosted flux distribution $P(S_p)$ for the two sources, GN 1200.3 and GN 1200.35.

Following Coppin et al. (2006), only sources with a posterior probability less than 5 per cent of having a flux density less than or equal to zero were retained in the final source catalogue. This means that of the two examples just employed, GN 1200.3 makes it into the final catalogue, whereas GN 1200.35 does not. Adopting this criterion leads to a total of 17 sources being discarded, all of them originally detected at below 4σ . The final revised source list is indicated through column seven of Table 1. We adopt the deboosted flux density as the value at which the $P(S_p)$ distribution peaks, with the errors calculated as the 68 per cent confidence bounds on the non-Gaussian deboosted flux distribution. On average, the deboosting reduces the observed fluxes by about 0.7 mJy, as shown in Fig. 6. In addition, the deboosting results in larger photometric errors and non-Gaussian probability distributions (see Fig. 5), particularly in cases where the photometric errors are already large.

The final catalogue of deboosted $\geq 3.5\sigma$ MAMBO sources consists of 30 sources. In §3.2.1 we found that seven of the 47 $\geq 3.5\sigma$ sources recovered prior to deboosting were spurious. Hence, of the sources in the deboosted list we expect $\sim 7 \times (30/47)$, or around four, to be spurious. This is almost certainly an upper limit since deboosting is designed to preferentially remove spurious sources. In Table 1 we list all of the original $\geq 3.5\sigma$ sources, because many of those which did not pass our deboosting criteria still have a reasonably high chance of being genuine and hence may be useful for follow-up studies at other wavelengths.

4 COMPARISON WITH THE SCUBA GOODS-N SURVEY

The SCUBA 850- μ m survey of the Hubble Deep Field North (HDF-N), which lies at the centre of the GOODS-N field, was one of the first extragalactic fields to be observed at submm wavelengths (Hughes et al. 1998; Serjeant et al. 2003) and to this day remains one of the deepest blank-field submm maps. A much larger, shallower 850- μ m image, covering most of the GOODS-N field, was presented by Borys et al. (2002) and this has been supplemented by several SCUBA jiggle maps (Holland et al. 1999) of other parts of GOODS-N (Borys et al. 2003, 2004; Wang et al. 2004; Pope et al. 2005; Pope et al. 2006). These data were combined into the so-called ‘super-map’ of GOODS-N by Borys et al. (2003), then updated in a series of subsequent papers. The resulting map combined the available data optimally, with the purpose of extracting point sources. The final version of the 850- μ m source catalogue was presented by Pope et al. (2006), with three new sources (GN 850.39, GN 850.40 and GN 850.41) presented by Wall, Pope & Scott (2008).

The AzTEC camera (Wilson et al. 2008) was used to survey the GOODS-N region at 1100- μ m (Perera et al. 2008). A comparison of the MAMBO and AzTEC millimetre maps will be explored in a future paper (Pope et al. in preparation).

In this section we will compare the 850- μ m super-map with our new 1200- μ m image, with two goals: first, to extract a robust sample of SMGs detected jointly at 850 and 1200 μ m; second, to compare the degree of overlap between the populations selected at each wavelength.

The optimal method for extracting sources of *arbitrary spectral shape* is to extract sources from the combined S/N map, thereby

Table 1. 1200- μm MAMBO sources extracted from the GOODS-N field at a significance $\geq 4\sigma$, with a supplementary list of sources with $3.5 \leq S/N < 4$ (italics). Sources which pass our deboosting criterion are assigned a deboosted flux density in the 7th column. These 30 sources make up our robust, deboosted catalogue, of which we expect no more than 3–4 to be spurious (§3.2.3). The three last columns list 1.4-GHz flux densities of all robust radio sources within a 6-arcsec radius of each MAMBO source, their mm-radio positional offset and the statistical significance of each mm-radio association, respectively. Associations with $P < 0.05$ are considered robust and are listed in boldface (see also § 5.4).

Name	GN name	R.A. (J2000)	Dec. (J2000)	$S_{1200\mu\text{m}} \pm \sigma_{1200\mu\text{m}}$ /mJy	S/N	$S_{1200\mu\text{m}}$ (deboosted) /mJy	$S_{1.4\text{GHz}}$ / μJy	offset /arcsec	P
MMJ123711+622211	GN 1200.1	12:37:11.7	+62:22:11	9.3 \pm 0.9	10.3	9.3 \pm 0.5	58 \pm 16	1.33	0.006
MMJ123633+621407	GN 1200.2	12:36:33.2	+62:14:07	4.9 \pm 0.7	6.95	4.4 \pm 0.7	34 \pm 4	2.28	0.017
MMJ123711+621328	GN 1200.3	12:37:11.2	+62:13:28	3.9 \pm 0.6	6.50	3.6 \pm 0.6	149 \pm 14	3.16	0.009
							62 \pm 6	5.92	0.047
MMJ123730+621258	GN 1200.4	12:37:30.8	+62:12:59	4.2 \pm 0.7	6.04	3.7 \pm 0.7	114 \pm 7	0.15	0.00006
MMJ123626+620604	GN 1200.5	12:36:26.9	+62:06:04	4.7 \pm 0.9	5.16	3.8 \pm 1.0	46 \pm 8	3.18	0.025
MMJ123714+621827	GN 1200.6	12:37:14.1	+62:18:28	3.6 \pm 0.7	5.08	2.9 \pm 0.8	627 \pm 8	2.33	0.002
MMJ123607+620855	GN 1200.7	12:36:07.8	+62:08:56	3.4 \pm 0.7	4.80	2.8 \pm 0.8
MMJ123702+621948	GN 1200.8	12:37:02.9	+62:19:48	3.3 \pm 0.7	4.67	2.7 \pm 0.8
MMJ123644+621940	GN 1200.9	12:36:44.6	+62:19:40	3.3 \pm 0.7	4.65	2.7 \pm 0.8
MMJ123737+621456	GN 1200.10	12:37:37.8	+62:14:56	2.8 \pm 0.6	4.60	2.2 \pm 0.7
MMJ123609+620648	GN 1200.11	12:36:09.7	+62:06:48	3.6 \pm 0.8	4.48	2.8 \pm 0.9
MMJ123550+621041	GN 1200.12	12:35:50.3	+62:10:42	4.5 \pm 1.0	4.48	3.5 \pm 1.2
MMJ123631+621715	GN 1200.13	12:36:31.8	+62:17:15	3.0 \pm 0.7	4.25	2.2 \pm 0.8
MMJ123635+620714	GN 1200.14	12:36:35.6	+62:07:14	3.0 \pm 0.7	4.25	2.2 \pm 0.8
MMJ123554+621338	GN 1200.15	12:35:54.0	+62:13:38	3.0 \pm 0.7	4.21	2.2 \pm 0.9	55 \pm 8	5.13	0.043
MMJ123723+622049	GN 1200.16	12:37:23.7	+62:20:49	3.3 \pm 0.8	4.15	2.3 \pm 1.0
MMJ123736+621103	GN 1200.17	12:37:36.0	+62:11:04	2.9 \pm 0.7	4.12	2.1 \pm 0.9	42 \pm 7	5.89	0.057
MMJ123556+621726	GN 1200.18	12:35:56.0	+62:17:26	3.3 \pm 0.8	4.07	2.3 \pm 1.0
MMJ123645+620823	GN 1200.19	12:36:45.1	+62:08:24	2.8 \pm 0.7	4.02	2.1 \pm 0.9
MMJ123749+621558	GN 1200.20	12:37:49.3	+62:15:59	2.8 \pm 0.7	4.00	2.1 \pm 0.9
3.5 $\leq \sigma < 4$ detections									
<i>MMJ123720+621106</i>	<i>GN 1200.21</i>	<i>12:37:20.8</i>	<i>+62:11:06</i>	<i>2.8 \pm 0.7</i>	<i>3.95</i>	<i>2.0 \pm 0.9</i>
<i>MMJ123711+620652</i>	<i>GN 1200.22</i>	<i>12:37:11.2</i>	<i>+62:06:52</i>	<i>3.9 \pm 1.0</i>	<i>3.92</i>
<i>MMJ123717+620800</i>	<i>GN 1200.23</i>	<i>12:37:17.4</i>	<i>+62:08:00</i>	<i>3.1 \pm 0.8</i>	<i>3.91</i>	<i>2.2 \pm 1.1</i>	97 \pm 19	4.24	0.021
<i>MMJ123755+621057</i>	<i>GN 1200.24</i>	<i>12:37:55.6</i>	<i>+62:10:58</i>	<i>3.5 \pm 0.9</i>	<i>3.91</i>
<i>MMJ123650+621217</i>	<i>GN 1200.25</i>	<i>12:36:50.9</i>	<i>+62:12:17</i>	<i>2.7 \pm 0.7</i>	<i>3.88</i>	<i>2.0 \pm 0.9</i>
<i>MMJ123643+622350</i>	<i>GN 1200.26</i>	<i>12:36:43.9</i>	<i>+62:23:51</i>	<i>4.7 \pm 1.2</i>	<i>3.87</i>
<i>MMJ123607+621137</i>	<i>GN 1200.27</i>	<i>12:36:07.2</i>	<i>+62:11:37</i>	<i>2.7 \pm 0.7</i>	<i>3.82</i>	<i>2.0 \pm 1.0</i>
<i>MMJ123605+621650</i>	<i>GN 1200.28</i>	<i>12:36:05.8</i>	<i>+62:16:50</i>	<i>2.7 \pm 0.7</i>	<i>3.80</i>	<i>2.0 \pm 1.0</i>
<i>MMJ123711+621218</i>	<i>GN 1200.29</i>	<i>12:37:11.8</i>	<i>+62:12:18</i>	<i>2.7 \pm 0.7</i>	<i>3.80</i>	<i>2.0 \pm 1.0</i>
<i>MMJ123638+622049</i>	<i>GN 1200.30</i>	<i>12:36:38.8</i>	<i>+62:20:50</i>	<i>3.0 \pm 0.8</i>	<i>3.78</i>
<i>MMJ123803+621446</i>	<i>GN 1200.31</i>	<i>12:38:03.4</i>	<i>+62:14:46</i>	<i>3.0 \pm 0.8</i>	<i>3.77</i>
<i>MMJ123711+621924</i>	<i>GN 1200.32</i>	<i>12:37:11.8</i>	<i>+62:19:24</i>	<i>2.6 \pm 0.7</i>	<i>3.75</i>	<i>1.9 \pm 1.0</i>
<i>MMJ123641+621129</i>	<i>GN 1200.33</i>	<i>12:36:41.9</i>	<i>+62:11:30</i>	<i>2.6 \pm 0.7</i>	<i>3.74</i>	<i>1.9 \pm 1.0</i>
<i>MMJ123752+621428</i>	<i>GN 1200.34</i>	<i>12:37:52.0</i>	<i>+62:14:28</i>	<i>2.6 \pm 0.7</i>	<i>3.70</i>
<i>MMJ123541+621150</i>	<i>GN 1200.35</i>	<i>12:35:41.7</i>	<i>+62:11:50</i>	<i>4.1 \pm 1.1</i>	<i>3.69</i>
<i>MMJ123802+621940</i>	<i>GN 1200.36</i>	<i>12:38:02.8</i>	<i>+62:19:40</i>	<i>4.4 \pm 1.2</i>	<i>3.68</i>
<i>MMJ123656+621647</i>	<i>GN 1200.37</i>	<i>12:36:56.8</i>	<i>+62:16:47</i>	<i>2.6 \pm 0.7</i>	<i>3.65</i>
<i>MMJ123540+621246</i>	<i>GN 1200.38</i>	<i>12:35:40.3</i>	<i>+62:12:47</i>	<i>3.7 \pm 1.0</i>	<i>3.65</i>
<i>MMJ123714+621842</i>	<i>GN 1200.39</i>	<i>12:37:14.1</i>	<i>+62:18:43</i>	<i>2.6 \pm 0.7</i>	<i>3.64</i>
<i>MMJ123745+621129</i>	<i>GN 1200.40</i>	<i>12:37:45.4</i>	<i>+62:11:30</i>	<i>2.5 \pm 0.7</i>	<i>3.61</i>
<i>MMJ123621+621705</i>	<i>GN 1200.41</i>	<i>12:36:21.5</i>	<i>+62:17:06</i>	<i>2.5 \pm 0.7</i>	<i>3.55</i>	...	138 \pm 7	2.86	0.008
							50 \pm 7	5.24	0.046
<i>MMJ123700+621453</i>	<i>GN 1200.42</i>	<i>12:37:00.6</i>	<i>+62:14:54</i>	<i>2.1 \pm 0.6</i>	<i>3.55</i>	<i>1.4 \pm 0.8</i>	53 \pm 13	5.84	0.051
<i>MMJ123712+621258</i>	<i>GN 1200.43</i>	<i>12:37:12.7</i>	<i>+62:12:59</i>	<i>2.1 \pm 0.6</i>	<i>3.55</i>	<i>1.4 \pm 0.8</i>
<i>MMJ123659+621619</i>	<i>GN 1200.44</i>	<i>12:36:59.2</i>	<i>+62:16:19</i>	<i>2.5 \pm 0.7</i>	<i>3.54</i>
<i>MMJ123653+622401</i>	<i>GN 1200.45</i>	<i>12:36:53.4</i>	<i>+62:24:01</i>	<i>4.2 \pm 1.2</i>	<i>3.53</i>
<i>MMJ123655+621408</i>	<i>GN 1200.46</i>	<i>12:36:55.5</i>	<i>+62:14:09</i>	<i>2.1 \pm 0.6</i>	<i>3.51</i>
<i>MMJ123557+621250</i>	<i>GN 1200.47</i>	<i>12:35:57.6</i>	<i>+62:12:50</i>	<i>2.5 \pm 0.7</i>	<i>3.51</i>

using all the information from the 1200- and 850- μm data. However, some care must be exercised, for at least two reasons. First, one is digging into the confusion noise in both images and hence non-Gaussianity or systematic artefacts in the maps may start to have effects that were not previously evident. Second, if one had strong prior information about the expected $S_{850\mu\text{m}}/S_{1200\mu\text{m}}$ ratio for the emitters then one would adopt a different weighting scheme.

The source-extraction method applied to the two maps individually (see Borys et al. 2003) is optimal, with the caveats given in § 3.1 for finding point sources, under the assumption that the noise distributions in both maps are Gaussian and uncorrelated.

The SCUBA super-map can be thought of as the answer to the question: ‘what is the best estimate of the flux density of a point source centred on each pixel?’. The super-map combines data taken in different observing modes, with different chop-throws, etc., and also takes into account the beam convolution in the process of fitting to the PSF. It follows that an efficient way of extracting point sources, using the information in both maps, is simply to treat the MAMBO image as additional data. These can then be combined with the SCUBA data to provide an overall S/N ‘map’, which gives the combined S/N level for a point source centred on each pixel. The relevant expression for each pixel is:

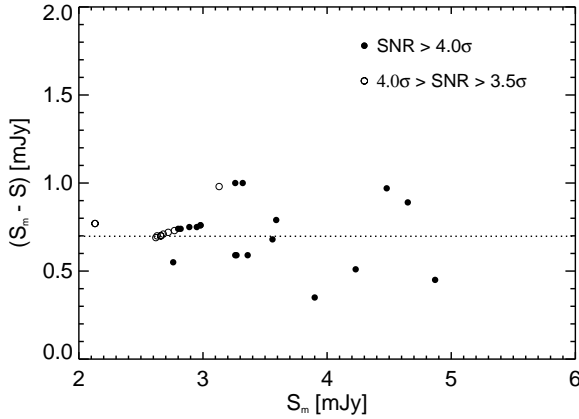


Figure 6. The difference between the raw and the deboosted 1200- μm flux densities as a function of the raw flux densities for sources in the final deboosted catalogue. On average, the raw flux densities are reduced by ~ 0.7 mJy as a result of the deboosting.

$$S = \frac{S_M/\sigma_M^2 + S_S/\sigma_S^2}{1/\sigma_M^2 + 1/\sigma_S^2}, \quad (3)$$

where σ_M and σ_S are the MAMBO and SCUBA noise maps, respectively. The corresponding noise map is

$$\sigma = \sqrt{\sigma_M^2 + \sigma_S^2}. \quad (4)$$

For this method to work straightforwardly, the two maps need to be astrometrically aligned and to have the same pixel scale and resolution. To this end, both maps were binned onto a 1-arcsec² pixel grid and we checked that no shift between the grids was required in order to maximise the correlation, then the MAMBO image was smoothed to the SCUBA resolution. We stress that this method only improves on the robustness of our detections, it does not provide estimates of the 850- and 1200- μm flux densities, which have to be measured from the separate maps.

Fig. 7 shows the combined 850- and 1200- μm S/N and r.m.s. noise maps obtained in this way, and Table 2 lists the sources extracted from the combined map.

A total of 13 (33) sources are detected above 5σ (4σ) in the combined map. In the bottom panel of Fig. 7, and in Table 2, we compare our dual-map source list with the SCUBA-only and MAMBO-only source lists. Any source from the combined map which has a $\geq 3.5\sigma$ deboosted MAMBO (SCUBA) source within 10 arcsec ($\sqrt{8^2 + 6^2}$ arcsec, where 8 and 6 arcsec are the 95-per-cent confidence limit for SCUBA and MAMBO sources (Iverson et al. 2005; Pope et al. 2006)) is deemed to have been *associated* at 1200 μm (850 μm).

How many sources have robust detections at both 850 and 1200 μm ? Only six sources from the combined list, four of which are detected at $\geq 5\sigma$ in the combined map, and one at 4σ . The sixth source, GN 1200.42 (GN 850.32), is detected at $\sim 3.8\sigma$. In cases with no detection at 850 or 1200 μm , we have determined 3σ upper flux density limits (Table 2). Finally, we note that one source detected at $\geq 4\sigma$ in the combined map, MM J123711+621245, was not previously known.

How big a fraction of the MAMBO and SCUBA sources are recovered in the combined map? All five (14) of the $\geq 5\sigma$ ($\geq 4\sigma$) MAMBO sources which lie within the SCUBA region are recovered in the combined map. Conversely, all of the $\geq 5\sigma$ SCUBA

sources are detected in the combined map, while for the $\geq 4\sigma$ SCUBA sources the corresponding fraction is 18/24 (75 per cent).

If we instead use Table 2 to answer the question ‘how big a fraction of the MAMBO sources have robust associations in the SCUBA map?’, we find that apart from the four $\geq 5\sigma$ MAMBO sources with SCUBA counterparts (a 100-per-cent recovery rate since the fifth $\geq 5\sigma$ MAMBO source, GN 1200.5, lies outside the SCUBA region) none of the other $\geq 4\sigma$ MAMBO sources have been recovered at 850 μm . This is clearly at odds with the high fraction of associations found for $\geq 4\sigma$ MAMBO sources by G04 in ELAIS N2 and Lockman Hole (~ 30 – 50 per cent) and the similarly high rate of associations for bright 1.1-mm BOLOCAM sources in the Lockman Hole (~ 75 per cent – Laurent et al. 2006). While positional uncertainties may go some way towards explaining the low fraction of associations in GOODS-N, the dominant factor is probably the mis-match in sensitivity of the MAMBO and SCUBA surveys in this region.

Finally, we note that GN 1200.4 – one of the brightest ($S_{1200\mu\text{m}} = 4.2 \pm 0.7$ mJy) and most significant ($\geq 5\sigma$) sources in our sample – is not detected at 850 μm and is thus a submm drop-out (SDO) candidate, although it does lie in a relatively noisy part of the SCUBA map.

5 THE 850-/1200-MICRON FLUX DENSITY RATIO

In this section we shall examine the 850- μm to 1200- μm flux density ($S_{850\mu\text{m}}/S_{1200\mu\text{m}}$) distribution of the (sub)mm sources in GOODS-N.

5.1 Sources detected by both SCUBA and MAMBO

We begin by considering the sources which are robustly detected by both MAMBO and SCUBA, i.e. sources which are in both of the deboosted source catalogues *and* detected at $\geq 4\sigma$ in the combined map. In total, only five such sources were found (see Table 2) and their resulting $S_{850\mu\text{m}}/S_{1200\mu\text{m}}$ versus 850- μm flux density distribution is shown in Fig. 8.

For comparison Fig. 8. also shows the robust MAMBO/SCUBA sample from E03, which are based on SCUBA photometry of MAMBO sources extracted from surveys of the Lockman Hole, the NTT Deep Field and the Abell 2125 cluster field (Bertoldi et al. 2000; Dannerbauer et al. 2002; 2004). Values of $S_{850\mu\text{m}}$ and $S_{1200\mu\text{m}}$ in E03 did not require deboosting as they were measured using ‘photometry mode’ (see Iverson et al. 1998b) at radio and/or mm interferometric positions. We also compare with the MAMBO/SCUBA samples derived from blank-field surveys of the ELAIS N2 and Lockman Hole fields by S02 and G04. For the five MAMBO/SCUBA associations found in the ELAIS N2 field, we derived $S_{1200\mu\text{m}}$ using the ‘deboosting curve’ given in G04, while a uniform deboosting factor of 15 per cent was adopted for $S_{850\mu\text{m}}$ (S02). In both cases, the deboosting factors were within the total flux calibration errors. Using a dual-survey extraction technique, Iverson et al. (2005 – hereafter I05) identified eight MAMBO/SCUBA associations in the Lockman Hole – in addition to the eight already presented by G04 – and we have included those in our comparison here. For all 16 associations in the Lockman Hole we have adopted $S_{850\mu\text{m}}$ (deboosted) from the SHADES survey (Coppin et al. 2006) which has a larger amount of data on the Lockman Hole than the UK 8-mJy Survey (S02). Deboosted $S_{1200\mu\text{m}}$ came from G04.

Although we have only identified five $\geq 4\sigma$

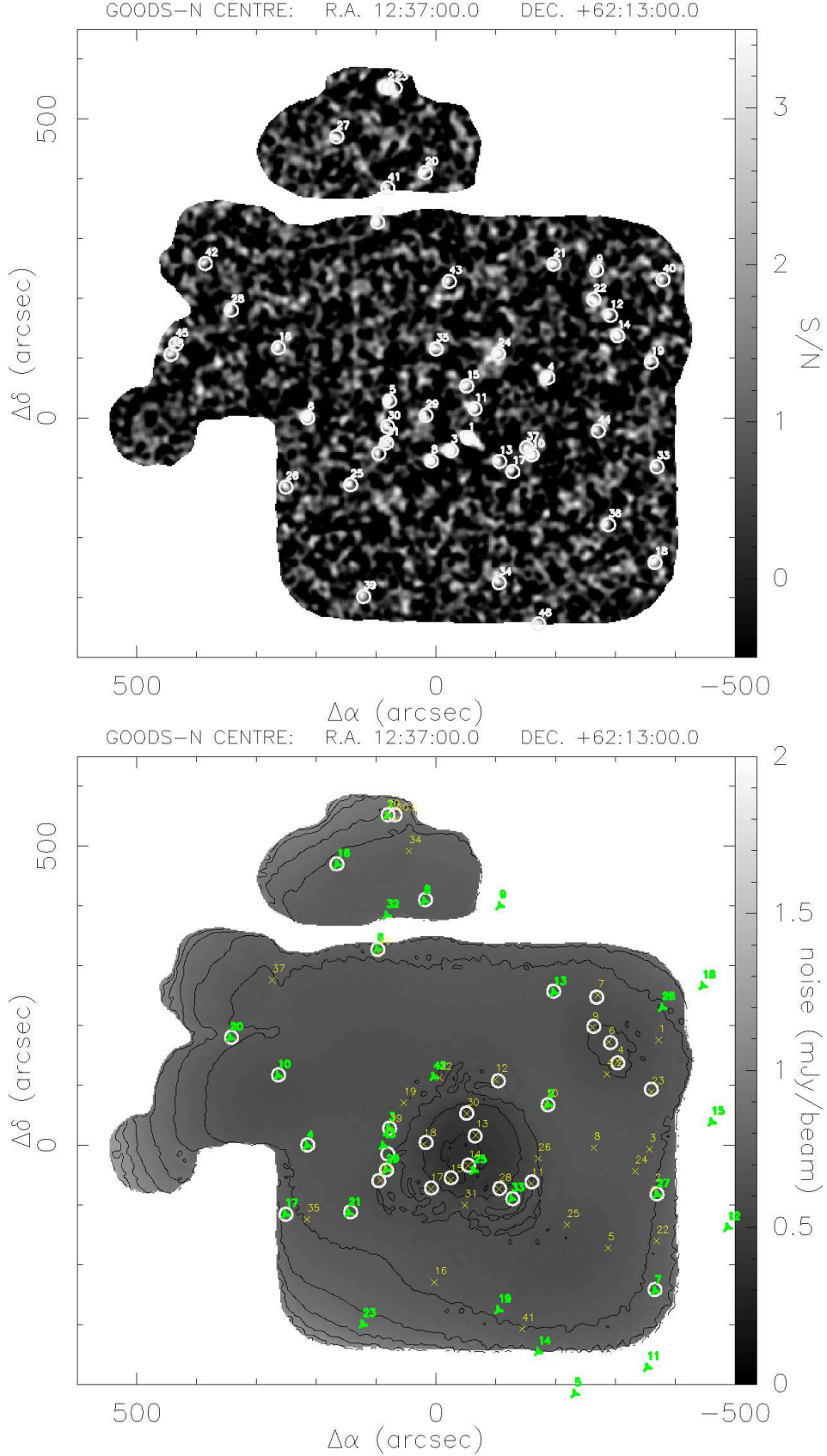


Figure 7. S/N image (top) and r.m.s. noise map (bottom) resulting from combining the 850- μm SCUBA map (Borys et al. 2003; Pope et al. 2005) and 1200- μm MAMBO map (this work) according to eqs 3 and 4. White circles indicate sources with $\geq 4\text{-}\sigma$ significance from the combined image. For the sake of clarity, these sources have not been numbered in the bottom panel. Green triangles indicate the deboosted $\geq 3.5\text{-}\sigma$ MAMBO sources in Table 1; yellow crosses are the deboosted $\geq 3.5\text{-}\sigma$ SCUBA sources, as given by Pope et al. (2006), with the addition of GN 850.39, .40 and .41 from Wall, Pope & Scott (2008).

Table 2. Sources extracted at $\geq 4\sigma$ from the combined 1200- and 850- μm image (eqs 3 and 4), with a supplementary list of sources extracted at $3.5 \leq S/N < 4$ (italics). The indices in parentheses refer to the numbering of the MAMBO catalogue in Table 1, except when there is no MAMBO association in which case we have started the index at 100. The same numbering is used in Fig. 7. The MAMBO and SCUBA associations in the second column from the left are those given in Table 1 and in Pope et al. (2005), respectively. Deboosted 1200- and 850- μm flux densities are given in parentheses in columns 6 and 7. In cases where no robust associations have been identified, we list the $3\text{-}\sigma$ upper flux density limit. Columns 8, 9 and 10 list $S_{1.4\text{GHz}}$ for all robust radio identifications within 8 arcsec of each MAMBO/SCUBA association in the combined map, the radial offset and the statistical significance of each radio identification, respectively. Identifications with $P < 0.05$ are considered robust and are given in boldface.

Name	GN name	R.A. (J2000)	Dec. (J2000)	S/N	$S_{1200\mu\text{m}} \pm \sigma_{1200\mu\text{m}}$ /mJy	$S_{850\mu\text{m}} \pm \sigma_{850\mu\text{m}}$ /mJy	$S_{1.4\text{GHz}}$ / μJy	offset	P
(100) MMJ123652+621226	GN 850.14	12:36:52.2	+62:12:26	14.7	≤ 2.1	5.9 ± 0.3 (5.9)	< 16
(1) MMJ123711+622212	GN 1200.1/GN 850.20	12:37:11.5	+62:22:12	13.5	9.3 ± 0.9 (9.3)	20.3 ± 2.1 (20.3)	58 ± 16	2.63	0.016
(101) MMJ123656+621205	GN 850.15	12:36:56.4	+62:12:05	8.75	≤ 2.0	3.7 ± 0.4 (3.7)	42 ± 6	3.02	0.024
(2) MMJ123633+621407	GN 1200.2/GN 850.10	12:36:33.2	+62:14:07	7.85	4.9 ± 0.7 (4.4)	11.3 ± 1.6 (11.3)	34 ± 4	2.28	0.017
(3) MMJ123711+621328	GN 1200.3/GN 850.39	12:37:11.1	+62:13:28	7.16	3.9 ± 0.6 (3.6)	7.4 ± 2.0 (5.2)	149 ± 14	3.42	0.010
(4) MMJ123730+621300	GN 1200.4	12:37:30.7	+62:13:00	6.14	4.2 ± 0.7 (3.7)	≤ 15.6	62 ± 6	6.57	0.053
(6) MMJ123714+621827	GN 1200.6/GN 850.40	12:37:14.0	+62:18:27	6.00	3.6 ± 0.7 (2.9)	13.1 ± 2.7 (10.7)	627 ± 7	1.16	0.0005
(102) MMJ123701+621148	GN 850.17	12:37:01.1	+62:11:48	6.00	≤ 2.0	3.9 ± 0.7 (3.9)	102 ± 12	3.31	0.014
(103) MMJ123621+621707	GN 850.7	12:36:21.5	+62:17:07	5.83	≤ 2.0	8.9 ± 1.5 (8.9)	138 ± 7	2.09	0.005
(104) MMJ123637+621158	GN 850.11	12:36:37.1	+62:11:58	5.83	≤ 2.0	7.0 ± 0.9 (7.0)	26 ± 5	3.19	0.028
(105) MMJ123650+621315	GN 850.13	12:36:50.7	+62:13:15	5.25	≤ 2.1	1.9 ± 0.4 (1.9)	47 ± 6	7.27	0.068
(106) MMJ123618+621551	GN 850.6	12:36:18.2	+62:15:51	5.00	≤ 2.0	7.5 ± 0.9 (7.5)	170 ± 7	1.08	0.001
(107) MMJ123644+621147	GN 850.28	12:36:44.8	+62:11:47	5.00	≤ 2.0	1.7 ± 0.4 (1.7)	90 ± 24	5.38	0.031
(108) MMJ123616+621517	GN 850.4	12:36:16.5	+62:15:17	4.83	≤ 2.0	5.1 ± 1.0 (4.9)	58 ± 7	4.13	0.031
(109) MMJ123652+621353	GN 850.30	12:36:52.7	+62:13:53	4.75	≤ 2.0	1.8 ± 0.5 (1.8)	20 ± 5	1.82	0.011
(10) MMJ123737+621457	GN 1200.10	12:37:37.7	+62:14:57	4.66	2.8 ± 0.6 (2.2)	≤ 6.0
(33) MMJ123641+621130	GN 1200.33	12:36:41.6	+62:11:30	4.60	2.6 ± 0.7 (1.9)	≤ 3.0
(7) MMJ123607+620858	GN 1200.7	12:36:07.8	+62:08:58	4.57	3.4 ± 0.7 (2.8)	≤ 19.4
(110) MMJ123608+621433	GN 850.23	12:36:08.5	+62:14:33	4.50	≤ 2.0	7.0 ± 1.9 (4.9)	48 ± 12	2.45	0.017
(8) MMJ123702+621950	GN 1200.8	12:37:02.6	+62:19:50	4.42	3.3 ± 0.7 (2.7)	≤ 10.7
(13) MMJ123631+621717	GN 1200.13	12:36:31.8	+62:17:17	4.42	3.0 ± 0.7 (2.2)	≤ 15.5
(111) MMJ123622+621618	GN 850.9	12:36:22.2	+62:16:18	4.33	≤ 2.0	8.9 ± 1.0 (8.9)	< 19.5
(112) MMJ123709+622212	GN 850.20.2	12:37:09.9	+62:22:12	4.22	≤ 2.7	11.7 ± 2.2 (9.9)	160 ± 9	6.45	0.024
(113) MMJ123645+621447	GN 850.12	12:36:45.1	+62:14:47	4.16	≤ 2.0	8.6 ± 1.4 (8.6)	103 ± 6	6.87	0.038
(21) MMJ123720+621108	GN 1200.21	12:37:20.4	+62:11:08	4.14	2.8 ± 0.7 (2.0)	≤ 10.0
(17) MMJ123735+621104	GN 1200.17	12:37:35.8	+62:11:04	4.14	2.9 ± 0.7 (2.1)	≤ 3.0	42 ± 7	7.0	0.061
(16) MMJ123723+622050	GN 1200.16	12:37:23.8	+62:20:50	4.00	3.3 ± 0.8 (2.3)	≤ 4.7
(20) MMJ123749+621560	GN 1200.20	12:37:49.0	+62:16:00	4.00	2.8 ± 0.7 (2.1)	≤ 23.9
(114) MMJ123702+621304	GN 850.18	12:37:02.4	+62:13:04	4.00	≤ 2.0	3.2 ± 0.6 (3.2)	21 ± 6	1.95	0.013
(115) MMJ123711+621245	...	12:37:11.5	+62:12:45	4.00	≤ 2.0	≤ 4.8
(29) MMJ123711+621218	GN 1200.29	12:37:11.8	+62:12:18	4.00	2.7 ± 0.6 (2.0)	≤ 4.0
(116) MMJ123713+621200	GN 850.21	12:37:13.7	+62:12:00	4.00	≤ 2.0	5.7 ± 1.2 (4.9)	34 ± 6	4.12	0.040
(27) MMJ123607+621138	GN 1200.27/GN 850.2	12:36:07.2	+62:11:38	4.00	2.7 ± 0.7 (2.0)	16.2 ± 4.1 (12.1)
<i>3.5 ≤ σ < 4 detections</i>									
(19) MMJ123645+620824	GN 1200.19	12:36:44.9	+62:08:24	3.85	2.8 ± 0.7 (2.1)	≤ 7.3
(42) MMJ123700+621455	GN 1200.42/GN 850.32	12:37:00.0	+62:14:55	3.83	2.1 ± 0.6 (1.4)	5.3 ± 1.4 (3.8)	53 ± 13	5.04	0.043
(117) MMJ123618+621001	GN 850.5	12:36:18.8	+62:10:01	3.83	≤ 1.9	6.7 ± 1.6 (5.2)	50 ± 15	4.14	0.034
(118) MMJ123638+621210	...	12:36:38.4	+62:12:10	3.80	≤ 2.0	≤ 5.9
(119) MMJ123803+621446	...	12:38:03.5	+62:14:46	3.75	≤ 2.1	≤ 2.5
(23) MMJ123717+620801	GN 1200.23	12:37:17.3	+62:08:01	3.75	3.1 ± 0.8 (2.2)	≤ 3.0	97 ± 19	3.38	0.015
(28) MMJ123605+621651	GN 1200.28	12:36:05.6	+62:16:51	3.71	2.7 ± 0.7 (2.0)	≤ 16.9
(32) MMJ123711+621924	GN 1200.32	12:37:11.5	+62:19:24	3.62	2.6 ± 0.7 (1.9)	≤ 10.9
(120) MMJ123755+621718	...	12:37:55.3	+62:17:18	3.62	≤ 2.1	≤ 46.4
(121) MMJ123656+621648	...	12:36:56.8	+62:16:48	3.57	≤ 2.6	≤ 4.6
(122) MMJ123621+621238	...	12:36:21.2	+62:12:38	3.57	≤ 2.0	≤ 14.5
(123) MMJ123802+621503	...	12:38:02.4	+62:15:03	3.50	≤ 2.0	≤ 15.1
(14) MMJ123635+620715	GN 1200.14	12:36:35.5	+62:07:15	3.50	3.0 ± 0.7 (2.2)	≤ 19.5	42 ± 13	7.60	0.073

MAMBO/SCUBA associations in GOODS-N, and therefore are dealing with small number statistics, the sources are seen to span a similar range in $S_{850\mu\text{m}}/S_{1200\mu\text{m}}$ and $S_{850\mu\text{m}}$ as existing samples. Most sources in all three samples exhibit a correlation between $S_{850\mu\text{m}}/S_{1200\mu\text{m}}$ and $S_{850\mu\text{m}}$. There are, however, a few outliers, although the uncertainties on some of these are substantial.

G04 (contrary to E03) did not find a significant fraction of sources with low $S_{850\mu\text{m}}/S_{1200\mu\text{m}}$ values, but there is no discrepancy between E03 and the G04+I05 sample compiled here.

This is due to the deboosted $S_{850\mu\text{m}}$ values and the wider and deeper coverage at 850 μm . As a result of the good agreement, we have combined all three samples in Fig. 8 in order to improve the statistics. The combined flux ratio distribution, shown as the empty histogram, is seen to be asymmetric around its peak at $S_{850\mu\text{m}}/S_{1200\mu\text{m}} \sim 2.5$, with 12 out of 48 sources (25 per cent) with $S_{850\mu\text{m}}/S_{1200\mu\text{m}} \geq 3$ and a shoulder of low $S_{850\mu\text{m}}/S_{1200\mu\text{m}}$ values, with 18/48 (38 per cent) of the sources lying at $S_{850\mu\text{m}}/S_{1200\mu\text{m}} \leq 2$.

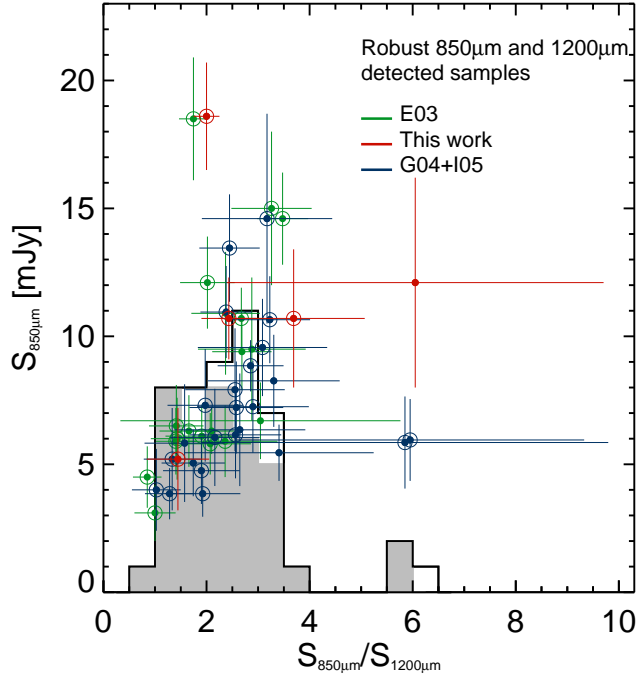


Figure 8. $S_{850\mu\text{m}}$ versus the $S_{850\mu\text{m}}/S_{1200\mu\text{m}}$ ratio, with corresponding uncertainties, for the deboosted sources identified in both the SCUBA and MAMBO source catalogues of the GOODS-N field (red symbols), the sample of 16 $\geq 3.5\text{-}\sigma$ SCUBA sources associated robustly with MAMBO in the Lockman Hole and ELAISN2 fields (blue symbols) and the sample of MAMBO sources with SCUBA photometry presented by E03 (green symbols). The open histogram shows the combined $S_{850\mu\text{m}}/S_{1200\mu\text{m}}$ distribution of all three samples, while the filled grey histogram shows the distribution for the subset of radio-identified sources.

5.2 Sources detected by MAMBO

Next we expand our sample to include the $\geq 4\text{-}\sigma$ MAMBO sources (20 sources – see Table 1) *plus* MAMBO sources which were detected at $\geq 4\sigma$ in the combined map (GN 1200.21, .27, .29, .33). The total tally is 18 sources within the SCUBA region, with six sources outside (see bottom panel of Fig. 7). In cases where there was no robust SCUBA association, we adopted the $3\text{-}\sigma$ limit in the $850\text{-}\mu\text{m}$ map at the position of the MAMBO source. The resulting plot of $S_{850\mu\text{m}}$ versus $S_{850\mu\text{m}}/S_{1200\mu\text{m}}$ is shown in Fig. 9a. The uneven noise properties of the SCUBA map are reflected in the large range of flux density ratios exhibited by the MAMBO sample. A handful of MAMBO sources in the shallowest parts of the SCUBA map have poorly constrained flux ratios ($\lesssim 10$). On the opposite side of the plot, we find three sources with tight upper limits on $S_{850\mu\text{m}}$, implying $S_{850\mu\text{m}}/S_{1200\mu\text{m}} \lesssim 2$. A number of such sources are also found when repeating the analysis for the ELAISN2 and Lockman Hole fields (S02+G04). For these two fields the SCUBA and MAMBO maps were well-matched in depth and, as a result, no sources with very high flux density ratios are found. Combining the S02+G04 results with those from GOODS-N, we obtain the open histogram shown in Fig. 9a. Accounting for the upper limits in the distribution, we find that 20–35 (37–65 per cent) of the 54 sources in the combined distribution lie at $S_{850\mu\text{m}}/S_{1200\mu\text{m}} \lesssim 2$ while 9–18 (17–33 per cent) have $S_{850\mu\text{m}}/S_{1200\mu\text{m}} \gtrsim 3$.

[h]

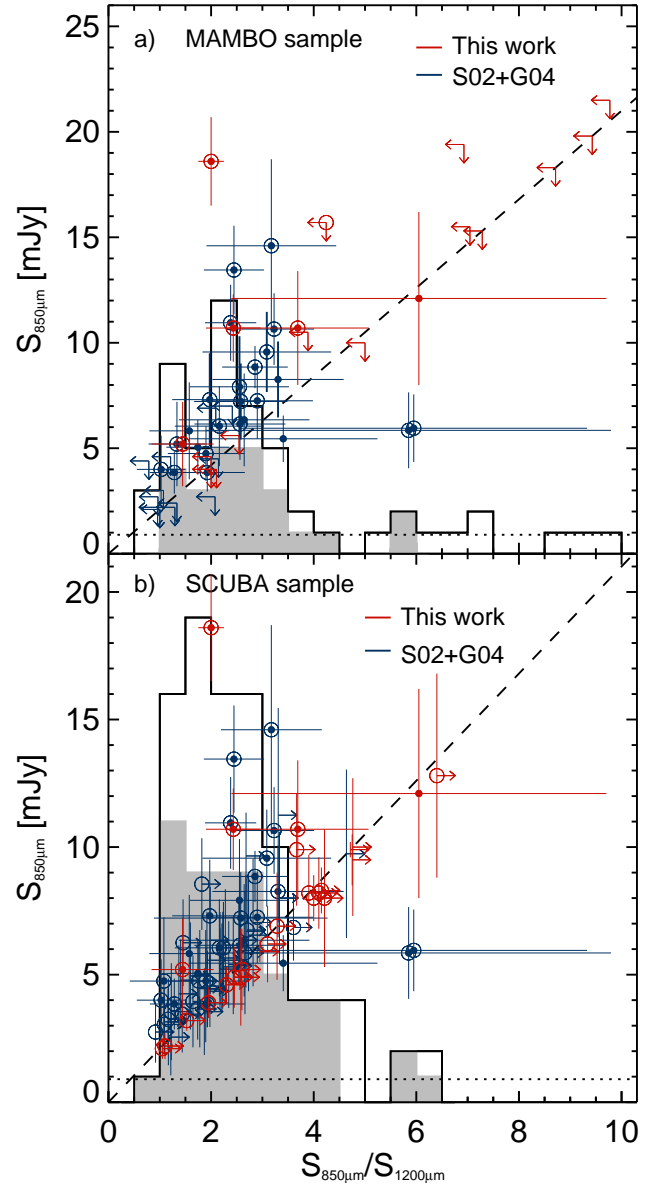


Figure 9. **a)** $S_{850\mu\text{m}}$ versus $S_{850\mu\text{m}}/S_{1200\mu\text{m}}$ for the entire $\geq 4\text{-}\sigma$ MAMBO sample and MAMBO sources detected at $\geq 4\sigma$ in the combined map (red symbols). For sources with no robust SCUBA association we used the $3\text{-}\sigma$ flux density limit at the MAMBO position in the SCUBA map. The sample of MAMBO sources obtained from the Lockman Hole and ELAISN2 fields (S02+G04) with SCUBA associations or upper limits on $S_{850\mu\text{m}}$ are also shown (blue symbols). The flux ratio distribution obtained by combining the two samples is given by the open histogram, while the distribution of radio-identified sources is shown as the grey histogram. **b)** The opposite experiment from a): $S_{850\mu\text{m}}$ versus $S_{850\mu\text{m}}/S_{1200\mu\text{m}}$ for the sample of $\geq 4\text{-}\sigma$ SCUBA sources in GOODS-N and SCUBA sources detected at $\geq 4\sigma$ in the combined map (red symbols). SCUBA sources from S02+G04 with MAMBO counterparts or $S_{1200\mu\text{m}}$ upper limits (3σ) are shown as blue symbols. The open histogram shows the flux ratio distribution for the combined GOODS-N and S02+G04 samples while the grey histogram shows the distribution for only radio identified sources (see §5.4). In both a) and b), the dotted line illustrates the $3\text{-}\sigma$ detection limit in the deepest part of the SCUBA map ($\sim 0.9\text{ mJy}$ – Pope et al. 2005), while the dashed line shows the value of $S_{850\mu\text{m}}$ corresponding to the $3\text{-}\sigma$ MAMBO detection limit ($\sim 2.1\text{ mJy}$) at a given flux density ratio.

5.3 Sources detected by SCUBA

As an important check, we performed the mirror-image experiment, deriving $S_{850\mu\text{m}}/S_{1200\mu\text{m}}$ for the SCUBA sample. We included all $\geq 4\sigma$ SCUBA sources (22 sources – Pope et al. 2006) and sources which were detected at $\geq 4\sigma$ in the combined map (GN 850.39, .23, .28, .30 and .40), yielding a total of 27 sources. As expected, most of the sources lie along the dashed line in Fig. 9b, which shows the flux density ratio corresponding to the 3σ detection limit of the MAMBO map (~ 2.1 mJy) for a given 850- μm flux density. The flux ratio distribution obtained by combining the GOODS-N sample with that of S02+G04 has a single dominant peak at $S_{850\mu\text{m}}/S_{1200\mu\text{m}} \sim 2 - 3$. Taking into account the lower limits in the combined distribution, we find that 10–37 (11–39 per cent) of the 94 sources in the distribution lie at $S_{850\mu\text{m}}/S_{1200\mu\text{m}} \leq 2$, while 26–74 (28–79 per cent) lie at $S_{850\mu\text{m}}/S_{1200\mu\text{m}} \geq 3$.

A Kolmogorov-Smirnov (KS) test of the flux density ratio distributions of the combined MAMBO and SCUBA samples in Fig. 9 yields a likelihood of ~ 46 per cent that identical distributions could differ by as much as that observed¹, i.e. the distributions are indistinguishable statistically. Nonetheless, we do note that 37–65 per cent of the sources in Fig. 9a have $S_{850\mu\text{m}}/S_{1200\mu\text{m}} \leq 2$ and 17–33 per cent have $S_{850\mu\text{m}}/S_{1200\mu\text{m}} \geq 3$, while the corresponding percentages in Fig. 9b are 11–39 and 28–79 per cent, respectively, i.e. the fractions are almost reversed between the two distributions.

Due to the uneven noise properties of the SCUBA map in particular, the non-negligible errors on the (sub)mm flux densities, and the small sample sizes, we are unable from Fig. 9 to make conclusive statements about any difference between the $S_{850\mu\text{m}}/S_{1200\mu\text{m}}$ distributions of MAMBO- and SCUBA-selected samples. However, we will reinvestigate this same question using two more fruitful approaches in § 6 and 7. But before doing so we will finish this section by examining whether radio identifications are helpful here.

5.4 850-/1200- μm flux ratio distribution of radio-bright and radio-dim (sub)mm sources

For the SCUBA samples in the Lockman Hole and ELAIS N2 regions we adopted the radio-identified SMGs in Ivison et al. (2002, 2007). For the SCUBA sample in GOODS-N, we adopted the radio identifications by Pope et al. (2005, 2006) and Biggs & Ivison (2006). To identify radio counterparts to our MAMBO sample in GOODS-N, we used the Biggs & Ivison (2006) radio catalogue to search for sources within 6 arcsec of each MAMBO source. For every such association, the probability, P , of this happening by chance was calculated using the method of Downes et al. (1986). A radio identification was considered robust if $P < 0.05$. In Tables 1 and 2, respectively, we list radio identifications for the catalogues extracted from the MAMBO data alone, and from the combined SCUBA/MAMBO map.

We find that only 9/30 (30 per cent) of the deboosted MAMBO sources have robust radio identifications, significantly lower than the typical identification fraction (65 per cent – e.g. Ivison et al. 2002) for bright SCUBA sources and radio data of similar depth ($\sigma_{1.4\text{GHz}} \sim 5 \mu\text{Jy beam}^{-1}$). Considering only the 1200- μm sources detected at $\geq 4\sigma$, the fraction increases although to no more than 35 per cent. If we instead consider the sample extracted at $\geq 4\sigma$ from the combined map (Table 2), we find 17/33 radio

identifications (52 per cent), roughly consistent with that of bright SCUBA sources.

From the combined samples in Fig. 8 we find that the fraction of MAMBO/SCUBA associations which also have radio identifications is roughly constant (~ 60 –100 per cent) across the range of flux ratios spanned by the combined sample. This is not surprising since we have only considered sources with high-S/N SCUBA and MAMBO detections. We therefore conclude that SMGs exhibit a broad range of $S_{850\mu\text{m}}/S_{1200\mu\text{m}}$ values, including quite low ratios, independent of whether or not they are identified at radio wavelengths.

Turning our attention to Fig. 9 and the flux ratio distributions of the MAMBO- and SCUBA-selected samples, and in particular the fraction identified at radio wavelengths as a function of flux density ratio (grey histograms), we find that at low flux density ratios ($S_{850\mu\text{m}}/S_{1200\mu\text{m}} \lesssim 2$) the fraction of MAMBO sources with radio identifications is 0–60 per cent, while the corresponding fraction for the SCUBA-selected sample is 47–100 per cent. Given that this fraction is expected to drop at $z \gtrsim 3$, this is the kind of scenario we would expect to see if 1200- μm observations were selecting a significant population at those redshifts. However, these are small number statistics; a formal KS test does not support the notion that the two populations differ, giving a 24 per cent chance that the two distributions are drawn from the same parent distribution.

6 STACKING ANALYSIS

As we saw in §4, only five $\geq 4\sigma$ sources in the combined map of the GOODS-N region are robustly detected at both 850- and 1200- μm . In this section we shall examine whether the remaining MAMBO (SCUBA) sources with no associations are detected at 850 μm (1200 μm) in a statistical sense.

To this end, we have carried out a 1200- μm stacking analysis of the 16 SCUBA sources in Table 2 with no MAMBO associations, but which were extracted from the combined SCUBA/MAMBO map at significance $\geq 4\sigma$. To avoid contamination by bright MAMBO sources and their negative sidelobes we produce a CLEANed version of the MAMBO map in which all the $\geq 3.5\sigma$ deboosted sources (including their negative sidelobes) were masked, as well as a region 11 arcsec in radius around each one. The 1200- μm signal and noise values were extracted from the MAMBO map at the positions of the SCUBA sources, and the (variance-weighted) mean flux density and noise values were derived. This yielded a total of 15 SCUBA sources with a stacked flux density of $\langle S_{1200\mu\text{m}} \rangle = 1.0 \pm 0.1$ mJy (S/N = 10). The average $S_{850\mu\text{m}}$ for these 15 SCUBA sources was 3.8 ± 0.2 mJy. As a check, we repeated the stacking analysis for the $\geq 3.5\sigma$ sample in Table 2 and found good agreement with the stacked flux density of the $\geq 4\sigma$ sample. As an extra check, we performed the stacking analysis with 10 per cent of the brightest and faintest of the 1200- μm flux density values removed from the stack, again finding agreement.

In a similar manner, we derived the stacked 850- μm flux density of the 11 MAMBO sources in Table 2 with no SCUBA associations, but which were recovered at $\geq 4\sigma$ from the combined map. To this end, we used the CLEANed version of the SCUBA signal map (Pope et al. 2005) to ensure the result would not be affected by the negative sidelobes around each source. A 15-arcsec region around each $\geq 3.5\sigma$ source was also blanked out. The final stack contained all 11 sources and yielded a stacked flux of $\langle S_{850\mu\text{m}} \rangle = 1.7 \pm 0.6$ mJy (S/N = 2.8). The average $S_{850\mu\text{m}}$ of

¹ In performing the KS tests between the MAMBO and SCUBA samples we have assumed that the upper and lower limits are measured values.

the 11 MAMBO sources was 2.4 ± 0.2 mJy. We found that the stacked $S_{850\mu\text{m}}$ for the $\geq 3.5\text{-}\sigma$ sample was consistent with the $\geq 4\text{-}\sigma$ sample and that removing the 10 per cent brightest and faintest sources from the stack did not change the result. Our stacking analysis is summarised in Table 3 where we have also listed the range in $S_{850\mu\text{m}}/S_{1200\mu\text{m}}$ implied by our analysis.

To gauge the significance of these results, we performed Monte Carlo simulations in which the stacked signal was determined in the same manner as above, except with randomised source positions. For the randomisation, we only considered positions within the MAMBO/SCUBA overlap region. Furthermore, since we wanted the simulations to represent similar noise properties to those in the original stacking analysis, each source was assigned a random position 20–80 arcsec from its original position. From 10,000 such runs – each time with different positions – we found that the observed 1200- μm signal occurs on ≤ 0.001 per cent of occasions, while there is a 4 per cent chance of obtaining the observed 850- μm stacked signal. This confirms the high significance of the stacked 1200- μm signal and suggests the 850- μm signal could occur by chance.

It is important to realise that these stacked fluxes are likely to be biased low, since the MAMBO and SCUBA maps are unlikely to be perfectly aligned and since the positional uncertainties of (sub)mm sources at low significance levels are ~ 4 arcsec. As a result, we repeated the entire stacking analysis, this time using the peak flux within 10 arcsec of each source in the stack, rather than the flux density at the exact position (see § 4 for the reason for choosing a 10-arcsec radius). This yielded a stacked flux of $\langle S_{1200\mu\text{m}} \rangle = 1.8 \pm 0.1$ mJy ($S/N = 18$) for the 1200- μm -blank SCUBA sources; for the 850- μm -blank MAMBO sources we found $\langle S_{850\mu\text{m}} \rangle = 4.0 \pm 0.7$ mJy ($S/N = 5.7$).

While this method yields an apparently significant 850- μm detection of the 850- μm -blank MAMBO sources, selecting the peak within 10 arcsec of each source will bias the stacked 850- μm flux density to high values. We consider the estimated signal from this method to represent an upper limit, so the average 850- μm flux density lies in the range $\langle S_{850\mu\text{m}} \rangle \simeq 1.7 - 4.0$ mJy. The SCUBA sample is detected significantly ($\geq 10\sigma$) at 1200 μm with both methods with $\langle S_{1200\mu\text{m}} \rangle \simeq 1.0 - 1.8$ mJy.

Stacked fluxes obtained by selecting peaks within a certain radius are prone to flux boosting. We therefore repeated the above analysis, this time deboosting the peaks using the Bayesian scheme described in § 3.2.3. This yielded a stacked flux of $\langle S_{1200\mu\text{m}} \rangle = 1.2 \pm 0.1$ mJy ($S/N = 12$) for the 1200- μm -blank SCUBA sources, while for the 850- μm -blank MAMBO sources we found $\langle S_{850\mu\text{m}} \rangle = 3.0 \pm 0.7$ mJy ($S/N = 4.3$). The net effect of deboosting is to lower the stacked flux estimates, narrowing the range in $\langle S_{850\mu\text{m}} \rangle / \langle S_{1200\mu\text{m}} \rangle$ for both the MAMBO and SCUBA samples (see Table 3).

In addition to the stacking analysis, we compared the distribution of 850- μm S/N values at the positions of the 850- μm -blank MAMBO sources with that of the overall S/N distribution of the (CLEANed and blanked) SCUBA map, and similarly compared the 1200- μm S/N distribution of the 1200- μm -blank SCUBA sources with the overall S/N distribution of the (CLEANed and blanked) MAMBO map (only considering the region overlapping with the SCUBA map). Comparing the full S/N distributions is likely to be a more robust method than calculating the stacked flux densities, which only uses the first moment. We performed this analysis for the 1200- μm -blank SCUBA sources and 850- μm -blank MAMBO sources which had been extracted at $\geq 2.5\sigma$ from the SCUBA and MAMBO maps, respectively. We stress that by ‘1200-

μm - (850- μm -)blank’, we mean sources which did not have a $\geq 2.5\text{-}\sigma$ MAMBO (SCUBA) association within 10 arcsec of its position in the combined map. The resulting distributions are shown in Fig. 10. The 1200- μm S/N distribution of the 1200- μm -blank SCUBA sources is clearly skewed towards positive values relative to the map. A KS test gives a 0.013 per cent likelihood that the two distributions are identical. For the 850- μm -blank MAMBO sources, the 850- μm S/N distribution is not strongly inconsistent with that of the overall SCUBA map (KS test probability, 4.5 per cent).

The statistical detection of the 1200- μm -blank SCUBA sources is consistent with these sources lying just below the detection threshold at 1200- μm , but being otherwise identical to the detected sources. The non-detection of the 850- μm -blank MAMBO sources – except when non-deboosted peak values are used in the stack – suggests that these sources lie *well* below the detection threshold, being much fainter than typical SMGs. These results are also reflected in the average $S_{850\mu\text{m}}/S_{1200\mu\text{m}}$ values. For the latter, $S_{850\mu\text{m}}/S_{1200\mu\text{m}} \lesssim 1.7$, while the 1200- μm -blank SCUBA sources have $S_{850\mu\text{m}}/S_{1200\mu\text{m}}$ values consistent with SMGs which have robust detections at both 850 and 1200 μm . Our findings therefore support the notion that a significant fraction of MAMBO sources selected from blank-field surveys are SDOs, with cooler 1200–850 μm colours.

7 SIMULATIONS OF THE ASSOCIATION FRACTIONS

Is the observed fraction of SCUBA sources with MAMBO associations (and vice versa) consistent with what we would expect given the properties of the maps? Since the noise varies significantly across the SCUBA map, we must address this question by means of careful Monte Carlo simulations of the associations, taking into account the varying depths of the SCUBA and MAMBO maps.

To this end, we took the $\geq 2.5\text{-}\sigma$ SCUBA and MAMBO catalogues and searched for counterparts within 10 arcsec of each other. In total, 28 such SCUBA/MAMBO associations were found in this manner: 63 per cent of the $\geq 4\text{-}\sigma$ SCUBA sources had 1200- μm associations; 30 per cent of the $\geq 4\text{-}\sigma$ MAMBO sources had 850- μm associations. From the 28 SCUBA/MAMBO associations, we constructed a $S_{850\mu\text{m}}/S_{1200\mu\text{m}}$ distribution (see Fig. 11a), taking into account the errors (assuming Gaussianity). If SCUBA and MAMBO sources – even at faint flux density levels – trace the same galaxy population, we would expect the $S_{850\mu\text{m}}/S_{1200\mu\text{m}}$ distribution for the $\geq 2.5\text{-}\sigma$ samples to be representative for all SCUBA and MAMBO sources at all significance levels. This is the null hypothesis we want to test.

First, we examined whether the observed fraction of SCUBA sources with MAMBO associations is consistent with what we would expect. We ran a Monte Carlo simulation in which we assigned a random flux density – drawn from the resampled 850- μm flux density distributions of $\geq 4\text{-}\sigma$ SCUBA sources (Fig. 11b) – to each member of the sample of $\geq 4\text{-}\sigma$ SCUBA sources detected with MAMBO at $\geq 2.5\sigma$. Then a $S_{850\mu\text{m}}/S_{1200\mu\text{m}}$ value was randomly selected from the $S_{850\mu\text{m}}/S_{1200\mu\text{m}}$ distribution, and the corresponding $S_{1200\mu\text{m}}$ was calculated.

Next, we identified the regions of the SCUBA map where each 850- μm flux density value could be detected at $\geq 4\sigma$, given the observed noise. Since the noise varies across the SCUBA map, so the suitable regions vary for each flux value. We then drew random noise values, $\sigma_{1200\mu\text{m}}$, from the noise distribution of the parts of the

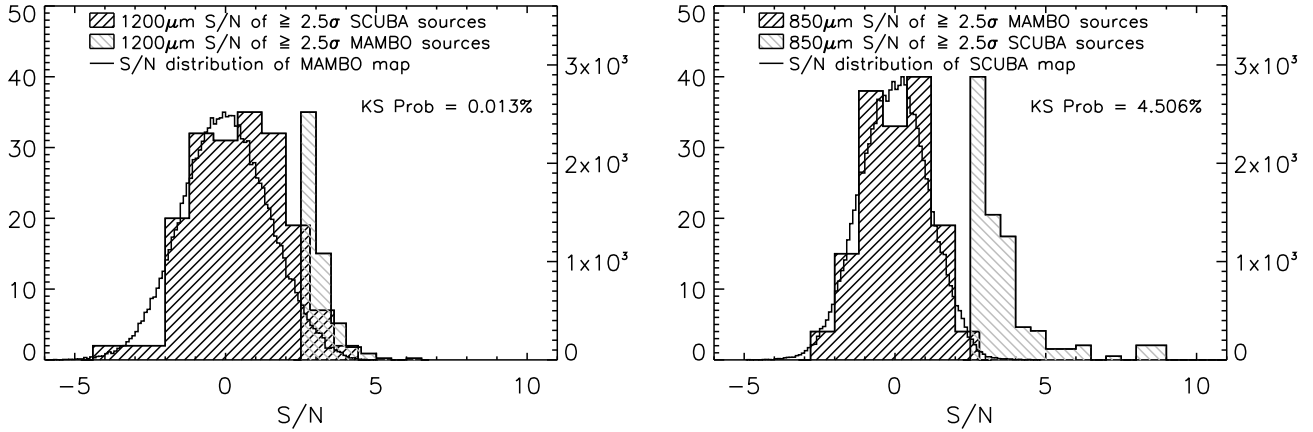


Figure 10. Left: Distribution of 1200- μm S/N values for the $\geq 2.5\text{-}\sigma$ SCUBA sources (hashed histogram and left y -axis) compared to the 1200- μm S/N distribution of the CLEANed and blanked MAMBO map (open histogram and right y -axis). The former is skewed towards positive values and a KS test yields a 0.013 per cent likelihood that the two distributions are identical. Also shown for comparison is the distribution of the 1200- μm S/N values of the $\geq 2.5\text{-}\sigma$ MAMBO sources (grey hashed histogram), normalised to the histogram for the $\geq 2.5\text{-}\sigma$ SCUBA sources. **Right:** Distribution of the 850- μm S/N values of the $\geq 2.5\text{-}\sigma$ MAMBO sources (hashed histogram and left y -axis), compared to the 850- μm S/N distribution of the CLEANed and blanked SCUBA map (open histogram and right y -axis). The two distributions are drawn from the same parent distribution with 4.5 per cent likelihood. For comparison, the 1200- μm S/N distribution of the $\geq 2.5\text{-}\sigma$ SCUBA sources is also shown (grey hashed histogram).

Table 3. Summary of stacking results for the 1200- μm -blank SCUBA sources and the 850- μm -blank MAMBO sources. Both the signals stacked using the flux densities at the (sub)mm centroids (biased low) and the peak flux densities within a 10-arcsec aperture (biased high) are listed. The last column lists the stacked signals obtained when deboosting the peak fluxes. The percentages in parentheses are the likelihoods of obtaining the stacked fluxes by chance.

1200- μm -blank SCUBA sources (N=15)			
	At centroid	Peak (measured)	Peak (deboosted)
$\langle S_{1200\mu\text{m}} \rangle / \text{mJy}$	$1.0 \pm 0.1 (< 10^{-3})$	$1.8 \pm 0.1 (< 10^{-3})$	$1.2 \pm 0.1 (< 10^{-3})$
$\langle S_{850\mu\text{m}} \rangle / \text{mJy}$	3.8 ± 0.2	3.8 ± 0.2	3.8 ± 0.2
$\langle S_{850\mu\text{m}} \rangle / \langle S_{1200\mu\text{m}} \rangle$	3.8 ± 0.4	2.1 ± 0.2	3.2 ± 0.3
850- μm -blank MAMBO sources (N=11)			
	At centroid	Peak (measured)	Peak (deboosted)
$\langle S_{1200\mu\text{m}} \rangle / \text{mJy}$	2.4 ± 0.2	2.4 ± 0.2	2.4 ± 0.2
$\langle S_{850\mu\text{m}} \rangle / \text{mJy}$	$1.7 \pm 0.6 (4)$	$4.0 \pm 0.7 (3)$	$3.0 \pm 0.7 (4)$
$\langle S_{850\mu\text{m}} \rangle / \langle S_{1200\mu\text{m}} \rangle$	0.7 ± 0.3	1.7 ± 0.3	1.3 ± 0.3

MAMBO map which overlapped with the suitable SCUBA regions. In doing this, we have accounted for the varying noise across the maps. An example of this is shown in Fig. 11c, where we show the regions of the MAMBO noise map which overlap with the regions in the SCUBA map where a flux density of 7.1 mJy is detectable at $\geq 4\sigma$. The noise distribution of this region is shown as the grey histogram in Fig. 11d.

Finally, the fraction of associations was calculated, based on how many sources had $S_{1200\mu\text{m}} / \sigma_{1200\mu\text{m}} \geq 2.5$. We ran this experiment 10,000 times, building up a distribution of association fractions, where by ‘association fraction’ we mean the fraction of SCUBA sources with associations in the MAMBO image. From the resulting distribution, shown in Fig. 11e, we see that the observed 1200- μm association fraction (63 per cent) is fully consistent (within 1σ) with the simulated distribution of association fractions (median, 75 per cent). We ran two additional simulations, sim-

ilar to that described above, but using the $\geq 3.5\text{-}\sigma$ and $\geq 5\text{-}\sigma$ SCUBA samples. In both cases, we found that the observed association fraction is consistent with the simulations. The observed fraction of SCUBA sources recovered at 1200 μm is expected, then, given the noise properties of the maps.

Can the same be said for the 850- μm recovery fraction of MAMBO sources? To test this, we carried out the mirror-image experiment as above, i.e. random 1200- μm fluxes were assigned to the sample of $\geq 4\text{-}\sigma$ MAMBO sources with $\geq 2.5\text{-}\sigma$ SCUBA detections, using the resampled $\geq 4\text{-}\sigma$ 1200- μm flux distribution (Fig. 11f). Using the same 850-/1200- μm distribution as above (i.e. derived from the $\geq 2.5\text{-}\sigma$ detections) the 850- μm flux densities were determined for the sample. In a similar manner as before, the regions of the MAMBO maps in which each 1200- μm flux density could be detected at $\geq 4\sigma$ were identified and 850- μm noise values were randomly extracted from the noise distributions of the

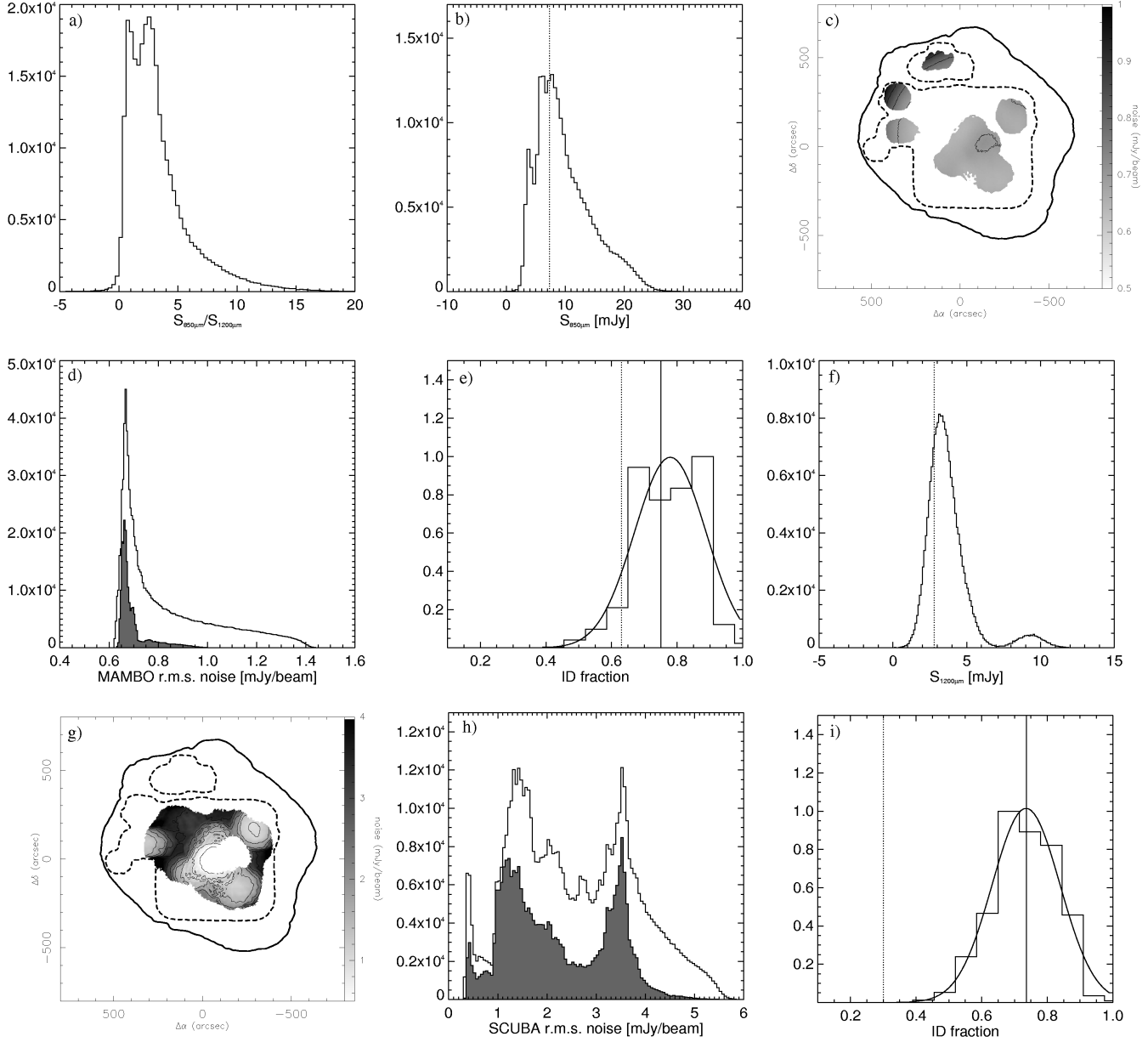


Figure 11. Distributions from our Monte Carlo simulations, described in §7. **a)** $S_{850\mu\text{m}}/S_{1200\mu\text{m}}$ distribution derived by resampling the flux density ratio distribution of the 28 SCUBA/MAMBO associations found as described in §7, taking into account the flux density errors. **b)** The 850- μm flux density distribution obtained by resampling the flux distribution of the $\geq 4\sigma$ SCUBA sources. The vertical dotted line represents a flux density of 7.1 mJy drawn from this distribution. **c)** The grey-scale regions show the parts of the MAMBO map which correspond to regions in the SCUBA map where a flux density of 7.1 mJy can be detected at $\geq 4\sigma$. This serves as an example of how we have taken the inhomogeneous noise distribution of the maps into account. **d)** The open histogram shows the noise distribution of the entire MAMBO map, while the noise distribution of the regions selected in **c)** are shown as a filled, grey histogram. **e)** The resulting 1200- μm association fraction distribution (normalised to unity) for the $\geq 4\sigma$ SCUBA sample. The vertical solid line indicates the median of the distribution (75 per cent), while the dotted line shows the actual observed fraction (63 per cent). The solid curve represents a single Gaussian fitted to the distribution. **f)** The flux density distribution of the $\geq 4\sigma$ MAMBO sample. The vertical dotted line represents a randomly chosen flux value of 2.8 mJy. **g)** The grey-scale regions show parts of the SCUBA noise map which correspond to regions in the MAMBO map where a flux density of 2.8 mJy can be detected at $\geq 4\sigma$. **h)** The noise distribution of the entire SCUBA map (open histogram), and the noise distribution corresponding to the noise regions shown in **g)** (filled, grey histogram). **i)** The 850- μm association fraction distribution (normalised to unity) for the $\geq 4\sigma$ MAMBO sample. The vertical solid line indicates the median of the distribution (74 per cent) and the dotted line shows the actual observed fraction (30 per cent).

matching regions in the SCUBA noise map. Finally, the fractions of associations were calculated. The resulting distribution of 850- μm association fractions for the $\geq 4\sigma$ MAMBO sources is shown in Fig. 11i and it is seen that the observed 850- μm association fraction (30 per cent) of MAMBO sources falls completely outside the simulated distribution of association fractions, deviating from the mean (74 per cent) by 4σ .

The conclusion of this analysis is that, provided we are prepared to use the sample of lower significance peaks, we can reject the null hypothesis for MAMBO sources. In other words there is evidence for a population of 1200- μm sources which does not share the distribution of flux density ratios with sources found jointly at 850 and 1200 μm . The non-trivial distribution shown in Figs. 11e and i underscores the importance of performing these careful Monte Carlo tests in order to be confident of this result. In order to explain the low fraction of associations, given the signal and noise properties of the two maps, the 850-/1200- μm flux density distribution for the MAMBO population would have to be skewed towards lower values. This argues in favour of a significant fraction of them being SDOs, at higher redshifts and/or with cooler dust.

8 DISCUSSION

The spectroscopic redshift survey of bright, radio-identified SMGs by Chapman et al. (2003, 2005) located sources out to $z \sim 3.6$, with an interquartile range, $1.7 \leq z \leq 2.8$. I05 argued that of the bright SMG population ($S_{850\mu\text{m}} \geq 5$ mJy), probably no more than ~ 10 per cent could be at $z > 3.5$, given that ~ 80 per cent have radio counterparts and ~ 10 per cent were likely to be spurious. Pope et al. (2006) reached a similar conclusion, estimating that ≤ 14 per cent of SMGs reside at $z \gtrsim 4$. Modeling the radio/mm/far-infrared colours of 120 SMGs from SHADES and adopting priors for the redshift probability of their radio-undetected sources, Aretxaga et al. (2007) argued that more than half of the bright SMG population lies in the range $1.6 \lesssim z \lesssim 3.4$, with little room for a $z > 4$ population. Thus, the evidence for a *significant* population of SMGs at very high redshifts appears slim, but has not been ruled out completely.

If we consider sources *strictly selected at 850 μm* , seven have spectroscopically confirmed redshifts in the range $3 \lesssim z \lesssim 3.6$ (Ledlow et al. 2002; Chapman et al. 2003, 2005). A strong candidate for a $z \gg 3$ SMG was reported by Knudsen, Kneib & Egami (2006) who inferred a likely spectroscopic redshift of $\simeq 4$ for SMM J16359+66130. Apart from this source, however, only one other convincing candidate for a $z > 4$ SMG has been presented in the literature at the time of writing, namely GN 850.10 (Wang et al. 2004; Pope et al. 2005). This source was deemed to reside at $z \sim 4 - 6$, based on its near- and mid-infrared colours, which were facilitated by its accurate location at 890- μm with the SMA (Wang et al. 2007), at 1.1 mm with the IRAM PdBI and in the radio with the VLA (Biggs & Ivison 2006; Dannerbauer et al. 2008). Younger et al. (2008) presented SMA observations of LH 850.2 – one of the brightest 850- μm (and 1200- μm) sources in the Lockman Hole (G04; Coppin et al. 2006) – and derived an optical/infrared photometric redshift of $z \simeq 3.3$, at the high-end of (but within) the Chapman et al. redshift distribution. Aretxaga et al. (2007) presented a handful of SMGs from SHADES with photometric redshifts $z \gtrsim 4$, but with very large individual uncertainties.

Turning our attention to sources *strictly selected at mm wavelengths*, we find a larger number of possible $z > 4$ candidates. Us-

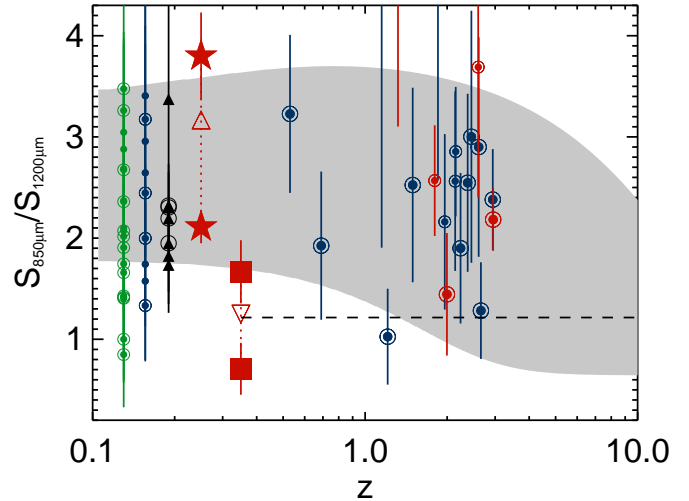


Figure 12. Green, blue and red filled circles represent $S_{850\mu\text{m}}/S_{1200\mu\text{m}}$ for sources identified robustly at 850 and 1200 μm by E03, S02+G04 and in this work, respectively. The filled triangles are the seven sources from Younger et al. (2007), where we have converted the measured 890- and 1100- μm flux densities to 850- and 1200- μm flux densities assuming an optically thin grey-body with $\beta = 1.5$. Sources which have robust radio counterparts have been circled. Where available, we have placed sources at their spectroscopic (Chapman et al. 2005) or photometric redshifts (Aretxaga et al. 2007; Pope et al. 2006; Wall, Pope & Scott 2008), otherwise the sources have been placed at fixed redshifts below $z = 0.3$ for clarity. Sources with spectroscopic redshifts are shown as large symbols while sources with only a photometric redshift – or lacking a redshift estimate entirely – are shown as small symbols. The grey shaded region corresponds to the range of $S_{850\mu\text{m}}/S_{1200\mu\text{m}}$ spanned by grey-bodies with $\beta = 1.0$ and $T_d = 10$ K (lower limit) and $\beta = 2.0$ and $T_d = 70$ K (upper limit). Large red squares and stars represent the range in $S_{850\mu\text{m}}/S_{1200\mu\text{m}}$ derived from the (centroid and peak) stacking analysis for the 850- μm -blank MAMBO sample and the 1200- μm -blank SCUBA sample, respectively. The open upward- and downward-pointing triangles represent the lower and upper limits on the flux density ratio, respectively, obtained when using deboosted peak values in the stacking analysis (see § 6).

ing IRAM PdBI to accurately locate their positions, Dannerbauer et al. (2002, 2004) presented three examples of bright ($S_{1200\mu\text{m}} \gtrsim 3.5$ mJy) MAMBO sources which, based on their radio, (sub)mm and near-infrared properties, were argued to lie at $z \gtrsim 4$. The non-detection of these sources with *Spitzer*/IRS spectroscopy (Valiante et al. 2007) is consistent with this claim. Younger et al. (2007) presented 890- μm interferometric SMA observations of seven very bright ($S_{1100\mu\text{m}} \geq 7.6$ mJy) AzTEC sources selected at 1100 μm and argued that the five radio-dim ($S_{1.4\text{GHz}} \leq 41$ μJy) sources in their sample were likely to reside at higher redshifts than the radio-identified sources due to their systematically higher submm-to-radio flux ratios, lower IRAC 3.6–8.0- μm flux densities and non-detections at 24 μm .

Common to all of these $z > 4$ candidates, whether they are SCUBA-, MAMBO- or AzTEC-selected sources, is that they are very bright (i.e. luminous) and have been detected at both submm and mm wavelengths. The trend that the high-redshift candidates tend to be very bright was first noted by Ivison et al. (2002), who from deep radio imaging of a large sample of SMGs found evidence that very bright ($S_{850\mu\text{m}} \gtrsim 8$ mJy) SCUBA sources tend to have higher submm-to-radio flux density ratios than less luminous SMGs, indicating that they are at higher redshifts (Carilli & Yun

1999) and that strong luminosity evolution may have taken place (see also Pope et al. 2006).

From the above summary (and following § 7), one wonders whether submm- and mm-selected sources are drawn from identical populations? Does the preponderance of $z > 4$ candidates amongst the mm-selected sources reflect a real difference between the two populations, or is this merely a coincidence? The multi-wavelength properties of mm-selected sources have been studied far less thoroughly than SMGs, because they were discovered more recently and are often thought to be mere mm-wave analogues to SMGs. In particular, no systematic spectroscopic surveys have been undertaken of mm-selected sources and their redshift distribution is therefore not known.

A related question is: why are all of the $z > 4$ candidates amongst the brightest (sub)mm sources known? Is this merely a selection effect, reflecting the fact that we can currently detect only the brightest sources with (sub)mm and radio interferometers, or does it reflect a genuine evolutionary effect (Wall, Pope & Scott 2007)?

In § 6 we showed that while the 1200- μm -blank SCUBA sources are statistically detected at 1200 μm ($S/N \sim 10$), the 850- μm -blank MAMBO sources are not robustly detected at 850 μm ($S/N \sim 2.8$). In Fig. 12 we plot $S_{850\mu\text{m}}/S_{1200\mu\text{m}}$ for these two samples, using the stacking results listed in Table 3. The ranges of possible values for the average $S_{850\mu\text{m}}/S_{1200\mu\text{m}}$ ratio for the two samples only barely overlaps, even when accounting for the high and low biases introduced when using the centroid and peak values, respectively (see §6). If we deboost the peak fluxes which go into the stack, the allowed ranges do not overlap at all. On average, therefore, the 850- μm -blank MAMBO sample has significantly lower $S_{850\mu\text{m}}/S_{1200\mu\text{m}}$ ratios than the 1200- μm -blank SCUBA sample.

The strongest support for this result was given in § 7, based on Monte Carlo simulations of the association fractions in the two maps. Since we are working in the low- S/N regime, the fraction of sources recovered in two different maps will never be unity, so it is crucial to simulate the experiments. Careful simulations are required because of the inhomogeneous noise in the maps. The main outcome of our Monte Carlo simulations is that while the fraction of SCUBA sources detected with MAMBO is consistent with the $S_{850\mu\text{m}}/S_{1200\mu\text{m}}$ distribution of sources found in both maps, there are more MAMBO sources *not* detected by SCUBA than would be expected. Since the simulations account for the noise properties of the two maps, we were able to estimate the fraction of MAMBO sources which are undetected by SCUBA (compared with the expectation if the populations were the same, but in the presence of the observed noise properties) and found this to be ~ 40 per cent.

Thus, we have presented strong evidence which suggests that – while there is substantial overlap between the 850- μm - and 1200- μm - selected sources in GOODS-N – the two populations *are not* identical. A significant fraction of the 1200- μm -selected sources are unaccounted for by the 850- μm data. Due to the statistical nature of our analysis and the careful way in which we have taken into account the uneven depths and noise properties of the two maps of the GOODS-N region, we are confident that this is a general result that reflects the existence of two distinct, albeit overlapping, populations.

We still need to establish whether SDOs are genuinely at $z \gtrsim 4$ or whether they have cooler dust temperatures at redshifts typical of radio-identified SMGs. Due to the degeneracy between dust temperature and redshift (Blain 1999), and without direct spectroscopic redshifts, it is not trivial to determine which of the two explanations is appropriate.

We note from Fig. 12 that if the typical SEDs of SDOs are given by $T_d = 10 \text{ K}$ and $\beta = 1.0$, which is believed to be extreme not only compared to starbursts at the present day but also to SMGs (Kovács et al. 2006), then their most likely average flux ratio ($S_{850\mu\text{m}}/S_{1200\mu\text{m}} \sim 1.2$) would indicate an average redshift of $z \sim 1.3$. One such source is seen in Fig. 12, namely Lock850.27/LH 1200.7 (G04; I05) which has a flux density ratio of ~ 1 and lies at $z = 1.21$. Given the general lack of spectroscopic redshifts for SMG samples, further examples of such sources may exist, making them viable candidates for SDOs. Adopting $T_d = 20 \text{ K}$ and $\beta = 1.5$, close to the coolest dust temperature measured for SMGs so far (Kovács et al. 2006), results in an average redshift of $z \sim 4.6$. If we assume that SDOs have SED properties similar to those of radio-identified SMGs, i.e. $T_d = 35 \text{ K}$ and $\beta = 1.5$ (Kovács et al. 2006), we find their average redshift to be ~ 9 , in the regime where the k -correction starts to become positive (Blain & Longair 1993).

In the first of the three scenarios outlined above, we note that the angular sizes of cool ($T_d \lesssim 25 \text{ K}$) SMGs at $z < 2$ should scale roughly as $\theta \sim (S_{850\mu\text{m}}/\text{mJy})^{1/2}$ (Kaviani et al. 2003) which would imply that SDOs have typical sizes of $\theta \sim 1.3$ arcsec (for $S_{850\mu\text{m}} = 1.7 \text{ mJy}$ – see Table 3), corresponding to a physical diameter of 11 kpc at $z = 1.5$. Thus if SDOs reside at $z \lesssim 2$ they would have larger physical sizes than those observed for SMGs ($\sim 4 \text{ kpc}$ – Tacconi et al. 2006; Biggs & Ivison 2008), but similar angular sizes (~ 1 arcsec). If SDOs predominantly lie at the same redshifts as SMGs ($z \sim 2.5$) but have cooler dust temperatures ($T_d \lesssim 25 \text{ K}$), their angular sizes would be larger by a factor of two (Kaviani et al. 2003). Thus, if SDOs are in fact very cool systems with a redshift distribution similar to SMGs (or peaking at lower redshift), we would expect them to be quite extended in high-resolution radio and mm images.

If some SDOs, on the other hand, lie in the range $z \sim 4 - 10$ and have typical dust temperatures in the range $T_d \sim 20 - 40 \text{ K}$, the expected angular and physical sizes are $\theta \sim 1.5 - 2.3$ arcsec and 6.4–18.0 kpc, respectively, inconsistent with the typical sizes measured for SMGs. Thus, if the Kaviani et al. (2003) results are applicable, it would suggest that *SDOs are very extended systems over a broad range of plausible dust temperatures and/or redshifts*. We note that high-resolution 1.3-mm interferometry of SDOs should be able to test this and may provide a useful way of discriminating between typical SMGs – generally compact at mm wavelengths ($\lesssim 1$ arcsec – Tacconi et al. 2006; Younger et al. 2007) and SDOs, which our analysis here suggest may be larger.

Observational evidence for such extended systems was recently uncovered by Daddi et al. (2008), who demonstrated the existence of gas-rich disks at $z = 1.5$ with physical sizes 2–3 times those of SMGs, as implied by CO observations as well as rest-frame UV light. Some of these *BzK* galaxies – so called for the way they are selected (Daddi et al. 2004) – have been detected at very faint flux levels at 1200- μm ($\sim 1.5 \text{ mJy}$ – Dannerbauer et al. 2005) and have similar star-formation efficiencies to those of local spirals, i.e. an order of magnitude smaller than SMGs. They could be candidates for the cold, extended ‘cirrus’ dust models proposed by Efstathiou & Rowan-Robinson (2003). Certainly, these properties seem to fit with those of SDOs, opening up the interesting possibility of an overlap between the two populations, with SDOs making up some fraction of the near-infrared-selected population at $z \sim 1.5 - 2.4$.

However, it seems clear from a growing number of in-depth studies, that some of the brightest mm- (and submm-)selected sources are almost certainly at $z > 4$ (Dannerbauer et al. 2002;

Wang et al. 2004; Younger et al. 2007). The same may be true for many of the SDOs, although we stress that one cannot rule out a scenario in which SDOs are predominantly cool, low-redshift sources.

Adopting the high-redshift scenario ($z \simeq 5$) for SDOs, and assuming $T_d = 20$ K, $\beta = 1.5$ and $S_{850\mu\text{m}} = 1.7 - 4.0$ mJy (Table 3), we find far-infrared luminosities and dust masses of $L_{\text{FIR}} = (1 - 2) \times 10^{12} L_\odot$ and $M_d = (3 - 8) \times 10^9 M_\odot$, respectively. In this scenario, SDOs are luminous and massive systems, despite being relatively fainter at submm wavelengths. The presence of such systems at $z \simeq 5$ (corresponding to ~ 1 Gyr after the Big Bang) would have implications for our understanding of galaxy formation and evolution. Due to their large masses and high redshifts, SDOs and SMGs at $z > 4$ would be potential candidates for galaxies caught in the act of collapsing early in the Universe's history (Eggen, Lynden-Bell & Sandage 1962).

9 SUMMARY

We have undertaken the first deep and uniform 1200- μm survey of the GOODS-N region, identifying 30 sources (after flux deboosting) in our image. By combining our 1200- μm MAMBO map with the existing 850- μm SCUBA data, we have extracted a robust sample of 33 sources (sub)mm sources detected at a combined $S/N \geq 4$.

The principal question we wanted to address in this paper was whether the 850- and 1200- μm selected sources constitute identical, or merely overlapping, populations. We performed three independent statistical analyses of the 850- and 1200- μm maps and their corresponding source catalogues.

The first – a simple comparison of the 850-/1200- μm flux density ratio distributions for the 850- μm - and 1200- μm -selected samples, suggests that a larger fraction of MAMBO sources have low values of $S_{850\mu\text{m}}/S_{1200\mu\text{m}}$ compared to the SCUBA sources. This method suffers, however, from small sample sizes and the effects of maps with uneven noise properties, and so we were unable to see a significant difference between the two populations.

However, using the other two methods – both of which take into account the uneven noise properties – we do find evidence to suggest that the source populations selected by MAMBO and SCUBA are not identical. The strongest evidence comes from our Monte Carlo analysis of the fractions of SCUBA galaxies with MAMBO associations, and vice versa, which showed that while the fraction of SCUBA sources with MAMBO associations was consistent with the map properties and the $S_{850\mu\text{m}}/S_{1200\mu\text{m}}$ distribution of sources robustly detected at both wavelengths, the fraction of MAMBO sources with SCUBA associations was significantly lower than expected. In fact, we found that about 40 per cent of the MAMBO sources were not recovered at 850 μm , thus lending strong evidence to the notion that the two populations are not identical.

We have argued that the average $S_{850\mu\text{m}}/S_{1200\mu\text{m}}$ of SDOs is significantly lower than the bulk of the SMG population, suggesting that these sources are either very cool or lie at higher redshifts. It would require extremely cold and unusual ($T_d \simeq 10$ K and $\beta \simeq 1$) far-infrared/mm SEDs to explain the presence of SDOs at low redshifts ($z \lesssim 2$). Nonetheless, examples of such sources do exist. We hint at a link between such cool, extended mm-selected sources and the near-infrared-selected population of BzK galaxies, which are known to be gas-rich yet have star-formation rates an order of magnitude lower than those of SMGs.

If we adopt more realistic SED parameters ($T_d \simeq 20$ K and

$\beta \simeq 1.5$) for SDOs, it would imply an average redshift of $z \gtrsim 4$, i.e. beyond the range probed by spectroscopic surveys so far. If this is the case, it is tempting to speculate that SDOs could be potential candidates for galaxies collapsing very early on in the Universe's history.

It should be stressed, however, that our analysis merely shows that SDOs are at generally higher redshifts (or are cooler) than SMGs. Extensive comparison with detailed models will be required in order to determine what range of redshift distributions are consistent with the available data. This was beyond the scope of the present study. This task will also be made much easier with additional information on these sources, particularly spectroscopic or optical/IR photometric redshifts. However, this first requires finding an identification of these SDOs at other wavelengths.

Deep interferometric observations at (sub)mm wavelengths sensitive enough to probe the faint flux levels of SDOs, are likely to become one of the most promising ways of furthering our understanding of SDOs. Such observations would allow us to identify near-/mid-infrared and optical host galaxies with which to constrain their redshifts. Due to the limited sensitivity of current (sub)mm interferometers, however, such studies have been limited to the brightest SMGs. With the new generation of wide-band receivers, and with ALMA on the horizon, studies of larger samples of SDOs are becoming feasible. Furthermore, the wide, deep, multi-colour surveys planned with SCUBA-2 and *Herschel* (and on a somewhat longer time-scale, with CCAT) may provide useful far-IR/submm photometric redshifts for huge samples of SDOs and SMGs (Hughes et al. 2002; Aretxaga et al. 2003). Armed with these redshift constraints, heterodyne receivers with extremely high bandwidth could be employed to search for redshifted CO and/or C II line emission. For a complete census of obscured star formation and AGN activity across cosmic time, we must determine the range of SED properties for (sub)mm-selected sources, along with their true redshift distribution. Our evidence that mm-selected galaxies may extend beyond $z = 4$ suggests that this may be an efficient way to select and study massive galaxy formation at the earliest times.

ACKNOWLEDGMENTS

We are grateful to the IRAM staff at Pico Veleta, in particular to Stephane Leon for his assistance with the pool observing. We thank Helmut Dannerbauer and Alejo Martínez Sansigre for discussions and for useful comments on the paper. We also thank the referee for a useful, thorough and swift response. AP and DS would like to thank the Natural Sciences and Engineering Research Council of Canada. AP also acknowledges support provided by NASA through the *Spitzer* Space Telescope Fellowship Program, through a contract issued by the Jet Propulsion Laboratory, California Institute of Technology under a contract with NASA.

REFERENCES

- Aretxaga I., Hughes D.H., Chapin E.L., Gaztañaga E., Dunlop J.S., Ivison R.J., 2003, MNRAS, 342, 759
- Aretxaga I. et al., 2007, MNRAS, 379, 1571
- Barger A.J., Cowie L.L., Sanders D.B., Fulton E., Taniguchi Y., Sato Y., Kawara K., Okuda H., 1998, Nature, 394, 6690
- Bertoldi F., Menten K.M., Kreysa E., Carilli C.L., Owen F., 2000, 24th meeting of the IAU, Joint Discussion 9, Manchester

- Biggs A.D., Ivison R.J., 2006, MNRAS, 371, 963
 Biggs A.D., Ivison R.J., 2008, MNRAS, 385, 893
 Blain A.W., Longair M.S., 1993, MNRAS, 264, 509
 Blain A.W., Ivison R.J., Smail I., 1998, MNRAS, 296, L29
 Blain A.W., 1999, MNRAS, 309, 955
 Blain A.W., Smail I., Ivison R.J., Kneib J.-P., Frayer D.T., 2002, PhR, 369, 111
 Borys C., Chapman S.C., Halpern M., Scott D., 2002, MNRAS, 330, L63
 Borys C., Chapman S.C., Halpern M., Scott D., 2003, MNRAS, 344, 385
 Borys C., Douglas S., Chapman S.C., Halpern M., Nandra K., Pope A., 2004, MNRAS, 355, 485
 Carilli C.L., Yun M.S., 1999, ApJ, 513, L13
 Chapman S.C., Blain A.W., Ivison R.J., Smail I., 2003, Nature, 422, 695
 Chapman S.C., Blain A.W., Ivison R.J., Smail I., 2005, ApJ, 622, 772
 Coppin K., Halpern M., Scott D., Borys C., Chapman S., 2005, MNRAS, 357, 1022
 Coppin K. et al., 2006, MNRAS, 372, 1621
 Daddi E., Cimatti A., Renzini A., Fontana A., Mignoli M., Pozzetti L., Tozzi P., Zamorani G., 2004, ApJ, 617, 746
 Daddi E., Dannerbauer H., Elbaz D., Dickinson M., Morrison G., Stern D., Ravindranath S., 2008, ApJ, 673, L21
 Dannerbauer H., Lehnert M., Lutz D., Tacconi L., Bertoldi F., Carilli C., Genzel R., Menten K., 2002, ApJ, 573, 473
 Dannerbauer H., Lehnert M., Lutz D., Tacconi L., Bertoldi F., Carilli C., Genzel R., Menten K., 2004, ApJ, 606, 664
 Dannerbauer H. et al., 2005, AN, 326, 525
 Dannerbauer H., Walter F., Morrison G., 2008, ApJ, 673, L127
 Downes A.J.B., Peacock J.A., Savage A., Carrie D.R., 1986, MNRAS, 218, 31
 Eales S., Bertoldi F., Ivison R.J., Carilli C.L., Dunne L., Owen F., 2003, MNRAS, 344, 169
 Efstathiou A. & Rowan-Robinson M., 2003, MNRAS, 343, 322
 Eggen O.J., Lynden-Bell D., Sandage A.R., 1962, ApJ, 136, 748
 Giavalisco M., et al., 2004, ApJ, 600, L93
 Greve T.R., Ivison R.J., Bertoldi F., Stevens J.A., Dunlop J.S., Lutz D., Carilli C.L., 2004, MNRAS, 354, 779
 Holland W.S. et al., 1999, MNRAS, 303, 659
 Hughes D.H. et al., 1998, Nature, 394, 241
 Hughes D.H. et al., 2002, MNRAS, 335, 871
 Ivison R.J., Smail I., Le Borgne J.-F., Blain A.W., Kneib J.-P., Bezecourt J., Kerr T.H., Davies J.K., 1998a, MNRAS, 298, 583
 Ivison R.J. et al., 1998b, ApJ, 494, 211
 Ivison R.J. et al., 2000, MNRAS, 315, 209
 Ivison R.J. et al., 2002, MNRAS, 337, 1
 Ivison R.J. et al., 2005, MNRAS, 364, 1025
 Ivison R.J. et al., 2007, MNRAS, 380, 199
 Kaviani A., Haehnelt M.G., Kauffmann G., 2003, MNRAS, 340, 739
 Knudsen K.K., Kneib J.-P., Egami E., 2006, In: Proceedings of the conference "Infrared Diagnostics of Galaxy Evolution", Pasadena
 Kovács A., Chapman S.C., Dowell C.D., Blain A.W., Ivison R.J., Smail I., Phillips T.G., 2006, ApJ, 650, 592
 Kreysa E. et al., 1998, SPIE, 3357, 319
 Laurent G.T. et al., 2006, ApJ, 643, L38
 Ledlow M.J., Smail I., Owen F.N., Keel W.C., Ivison R.J., Morrison G.E., 2002, ApJ, 577, L79
 Perera T. et al., 2008, MNRAS, submitted
 Pope A., Borys C., Scott D., Conselice C., Dickinson M., Mobasher B., 2005, MNRAS, 358, 149
 Pope A. et al., 2006, MNRAS, 370, 1185
 Scott S.E. et al., 2002, MNRAS, 331, 817
 Serjeant S. et al., 2003, MNRAS, 344, 887
 Smail I., Ivison R.J., Blain A.W., 1997, ApJ, 490, L5
 Smail I., Ivison R.J., Owen F.N., Blain A.W., Kneib J.-P., 2000, ApJ, 528, 612
 Spergel D.N. et al., 2003, ApJS, 148, 175
 Tacconi L.J. et al., 2006, ApJ, 640, 228
 Valiante E., Lutz D., Sturm E., Genzel R., Tacconi L.J., Lehnert M., Baker A., 2007, ApJ, 660, 1060
 Wall J.V., Pope A., Scott D., 2008, MNRAS, 383, 435
 Wang W.-H., Cowie L.L., Barger A.J., 2004, ApJ, 613, 655
 Wang W.-H., Cowie L.L., Barger A.J., 2006, ApJ, 647, 74
 Wang W.-H., Cowie L.L., van Sadlers J., Barger A.J., Williams J.P., 2007, ApJ, 670, L89
 Wilson G.W. et al., 2008, MNRAS, 386, 807
 Younger J.D., et al., 2007, ApJ, 671, 1531
 Younger J.D., et al., 2008, MNRAS, in press
 Zylka R., 1998, Pocket Cookbook for the MOPSI Software. <http://www.iram.es/IRAMES/otherDocuments/manuals/Datared/pockcoo.ps>